Cancer associated talin point mutations disorganise cell adhesion and migration

Latifeh Azizi[1], Alana R. Cowell[2], Vasyl V. Mykuliak[1], Benjamin T. Goult[2*], Paula Turkki[1,3*], Vesa P. Hytönen[1,3*]
[1]BioMediTech, Faculty of Medicine and Health Technology, Tampere University
[2]School of Biosciences, University of Kent, Canterbury, Kent, CT2 7NJ, UK.
[3]Fimlab Laboratories, Tampere, Finland

Corresponding authors: Benjamin T. Goult: B.T.Goult@kent.ac.uk, Paula Turkki: paula.turkki@tuni.fi, Vesa P. Hytönen: vesa.hytonen@tuni.fi

Abstract

Talin-1 is a key component of the multiprotein adhesion complexes which mediate cell migration, adhesion and integrin signalling and has been linked to cancer in several studies. In this study we analysed mutations in talin-1 reported in the Catalogue of Somatic Mutations in Cancer. A total of 11 talin mutants were selected and expressed in talin-deficient fibroblasts and their functional and structural effects were characterised in detail. An I392N point mutation in the F3 domain caused a three-fold increase in invasion, and enhanced migration compared to wildtype talin. Mutations R1368W and L1539P in the R7 and R8 domains caused increased invasion and proliferation and affected talin-vinculin complexation, but were not linked to changes in their binding affinities with known substrates KANK1 and RIAM measured for isolated talin domains. Lastly, L2509P, a mutation in the dimerisation domain of talin, prevented talin dimer formation, actin recruitment and FAKpTyr397 activation leading to anisotropic cell spreading and loss of random migration. Altogether, this study suggests that cancer derived point mutations in talin-1 can drastically affect cell behaviour and so may contribute to cancer progression.

Keywords: talin, COSMIC, somatic mutations, cancer, migration, invasion, focal adhesion

Introduction

For cells to maintain homeostasis and co-operate within tissues, they need to dynamically interact with the extracellular matrix (ECM). In recent years the role of the microenvironment has become increasingly recognised (Lu et al., 2012) and disturbances between cell-ECM interactions, intracellular signalling events, and signals derived from the ECM have been shown to contribute to cancer progression. Talin is a major component of focal adhesions (FAs), responsible for mediating the link between the ECM via integrins and the actin cytoskeleton. Talin is a large ~250 kDa mechanosensitive protein consisting of an N-terminal FERM head domain (F0, F1, F2, F3; residues 1-405) followed by a linker (~80aa) and ~2000aa rod region comprised of 13 domains (R1 to R13) ending in a C-terminal dimerisation domain (DD) (Goult,Zacharchenko et al., 2013). The FERM domain interacts with the membrane-proximal NPxY motif of beta integrin tail and the negatively charged plasma membrane (Anthis et al., 2009;Tanentzapf and Brown, 2006). The rod domain contains two F-actin binding sites (ABS2 and ABS3) (Atherton et al., 2015;Gingras et al., 2008;Hemmings et al., 1996), 11 vinculin binding sites (VBS) (Gingras et al., 2005) and binding sites for regulatory proteins such as RIAM, KANK (Bouchet et al., 2016;Sun,Tseng et al., 2016) and the tumour suppressor DLC1 (Haining et al., 2018;Zacharchenko et al., 2016). Studies have shown that ABS3 is essential for FA assembly (Kopp et al., 2010), whereas ABS1 and ABS2 have a reinforcing role (Kumar et al., 2016;Sun,Guo et al., 2016).

Talin is the main scaffold protein in focal adhesions which form at the leading edge of a polarised cell. Talin links the intracellular tails of integrins to the actin cytoskeleton and mechanical forces exerted on talin can disrupt and reveal binding sites leading to formation of mature multiprotein FA complexes (Goult et al., 2018). These are dynamic processes regulated by a complex signalling network, gathering information from intracellular and extracellular events. The mechanical properties of the ECM are reflected by intracellular changes via the FA's and actomyosin network, having a direct effect on cell behaviour, such as cell shape, migration and proliferation (Makoto Nagano et al., 2012;Murrell et al., 2015).

Talin-1 overexpression has been shown to correlate with increased invasion and decreased survival with oral squamous cell carcinoma (Lai et al., 2011) as well as migration, invasion and anoikis resistance in prostate cancer cells (Sakamoto et al., 2010). Loss of talin-1 leads to diminished *in vivo* metastasis of prostate cancer cells via FAK-Src complex and AKT kinase signalling (Sakamoto et al.,

2010). Conversely, the downregulation of talin-1 has also been shown to promote hepatocellular carcinoma progression (Chen et al., 2017).

The COSMIC (Catalogue Of Somatic Mutations In Cancer) database (Tate et al., 2019) contains exon sequencing data of human cancers and provides a vast resource of somatic mutation information. In light of talins integral role in regulating cell behaviour, integrin adhesion signalling and its connection to cancer progression, we sought to explore how cancer-associated talin mutations may alter talin function and the behaviour of cells.

Results

Most cancer-derived point mutations of talin-1 do not appear to be deleterious and have limited influence on cell morphology and polarisation

To investigate functional consequences of talin-1 point mutations, 368 talin-1 mutations in COSMIC database (accessed January 2017) were evaluated, and 258 missense mutations were further screened using bioinformatic tools (Fig.1A). Eleven of these mutations were selected for further analysis based on the predicted potential to impact structural and functional properties of talin-1.

We investigated each of the 258 point mutations individually and determined the position of the mutation within the talin structure (Fig.1B). The pathogenicity of the amino acid substitutions were predicted using the PON-P2-algorithm (Niroula et al., 2015), which predicted the mutations in Table 1 to be pathogenic. We used a BLOSUM62 substitution matrix (Henikoff and Henikoff, 1992) and CBSM60 matrix (Liu and Zheng, 2006) to obtain a numeric penalty for each amino acid deviation and to predict the protein structure/function, respectively. Next we investigated if the mutations cause changes in amino acid polarity as the stability of talin domains are strongly dependent on hydrophobic effect (Fillingham et al., 2005;Isenberg et al., 2002). The degree of evolutionary conservation of the amino acids in the talin sequence was investigated using ConSurf (Ashkenazy et al., 2016). Finally, we evaluated if the mutation is close to known ligand-binding sites. All these factors were used to build a scoring coefficient and the weight for each variable was obtained using the manual iteration process described in the Supplementary material. Using this scoring, a final eleven mutations were selected for further investigation with the E1770Q mutation also included despite a lower score due to its location in the previously defined talin autoinhibition site (Goult et al., 2009;Haage et al., 2018)(Table1; Fig.1B).

Table 1. The list of talin-1 point mutations selected from the COSMIC database. In each column a normalised value close to 1 predicts defects in protein function. BH=mutation located between helices and DD=dimerisation domain. CBSM60= conformation-specific amino acid substitution matrix. BLOSUM62=BLOcks SUbstitution Matrix.

Talin-1 mutant	Recurrence	Primary tissue	Histology	Domain	Location	PON-P2 probability of pathogenicity	Normalised BLOSUM 62-matrix score	Normalised CBSM60 matrix score	Normalised ConSurf score	Final score
P229L	1	Skin	Carcinoma	F2	BH/buried	0.94	1	1	1	8.20
I392N	1	Pancreas	Carcinoma	F3	Buried	0.86	1	0.83	1	8.95
V577D	1	Liver	Carcinoma	R1	Buried	0.94	1	1	0.60	8.39
A893E	2	Central nervous system/pituitary	Glioma/Cranio pharyngioma	R3	BH/buried	0.95	0.75	0.33	0.60	7.63
R1368W	2	Hematopoietic and lymphoid tissue /large intestine	Lymphoid neoplasm /carcinoma	R7	Surface	0.98	1	1	1	7.75
Y1389C	2	Liver	Carcinoma/carcinoma	R7	Buried	0.90	0.87	0.67	1	8.58
L1539P	1	Liver	Carcinoma	R8	Buried	0.98	1	1	0.60	8.45
S1750F	1	Skin	Malignant melanoma	R9	Buried	0.89	0.87	0.5	0.60	7.55
E1770Q	1	Breast	Carcinoma	R9	Surface	0.81	0.37	- 0.33	1	6.01
D2086V	1	Breast	Carcinoma	R11	Surface	0.96	1	1	1	7.71
L2509P	1	Large intestine	Carcinoma	DD	DD /Surface	0.96	1	1	0.64	7.46

We evaluated the selected COSMIC mutations against the 1000 Genomes Project database, which is a large database of human genetic variant data (Clarke et al., 2012). Five of the eleven mutations were not found from the 1000 Genomes (P229L, I392N, L1539P, E1770Q and D2086V) and the other six were references only to the COSMIC database, indicating that these mutations have not been found in healthy individuals.

We transiently transfected talin double knock-out ($TLN1^{-/-}TLN2^{-/-}$) mouse embryonic fibroblasts (MEF) (Theodosiou et al., 2016) with talin-1 constructs containing the mutations shown in Table 1. To evaluate the effect the mutations have on cell morphology, we visualised talin and vinculin in transfected cells (Fig.1C) and quantified the effect of the mutations on cell area and circularity (Fig.2A,B). Many of the mutations caused little variance on cell morphology when compared to WT, except for cells carrying the dimerisation domain (DD) mutation L2509P, which were significantly smaller than the WT expressing cells and showed a more circular cell phenotype, indicating a loss in cell polarisation.

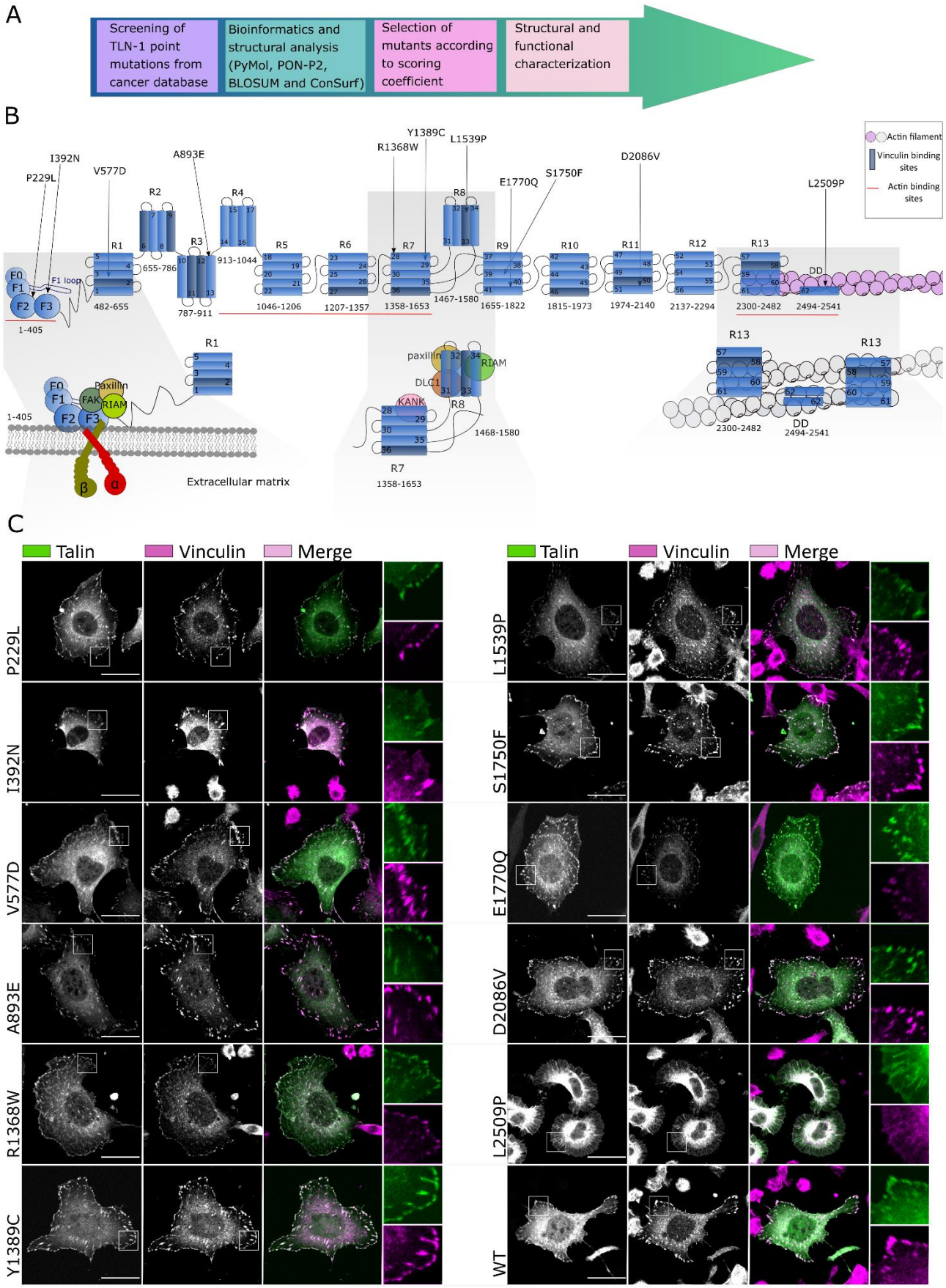

Figure 1: Out of 258 talin-1 mutations found from COSMIC, eleven were selected for further detailed studies. A) Flowchart showing the pipeline and bioinformatics tools used to select the eleven mutants from the COSMIC database investigated. B) Schematic representation of talin-1 and the positions of the selected missense mutations. C) SUM

projections of z-stacks of cells expressing GFP-tagged talin-1 (WT and/or point mutated) and immunolabeled for vinculin. Scale bars are 25 µm, zoom-in square size is 12.5µm x 12.5 µm.

Western blot analysis ensured translation of full-length proteins (Fig.S1B). The expression levels showed decreased expression for I392N and slightly increased expression for S1750F and D2086V but otherwise the expression levels were constant as cells were transfected with equal amounts of expression plasmids (Fig.S1A). The adhesion size and abundance were analysed from the cell periphery, and did not reveal significant changes in the adhesion area and number between cells transfected with various talin mutations (Fig.S2A,B).

We then set out to determine whether the talin mutants affected the expression levels of the well-characterised adhesion markers vinculin, paxillin, and the phosphorylation level of FAKpTyr397. Vinculin expression level was not majorly influenced by the expression of the talin-1 mutants. In contrast, expression of the talin mutants, P229L, V577D, A893E, L1539P and D2086V led to lower levels of paxillin expression when compared to WT-talin expressing cells (Fig.2C,D).

We further assessed the levels of vinculin, and paxillin within the talin-1 rich adhesion sites with the aid of immunofluorescence labelling and confocal imaging (Fig.2E,F). Interestingly, several mutants showed decreased levels of these FA components within the adhesion sites compared to cells expressing WT talin-1. Furthermore, the mutants R1368W and L1539P showed significantly less recruitment of both FA components analysed here. FAKpTyr397 is a marker for adhesion maturation and corresponds with mechanical activation of talin and is therefore present only at low level in the non-transfected talin double knock-out MEF cells (Rahikainen et al., 2019) enabling us to monitor the levels with western blotting (Fig.2G). As indicated by the anisotropic spreading of cells carrying the L2509P mutation, FAKptyr397 levels were decreased when compared to WT talin expressing cells. Mutants Y1389C and L1539P showed increased FAKpTyr397 levels when compared to WT expressing cells, suggesting increased FAK activity.

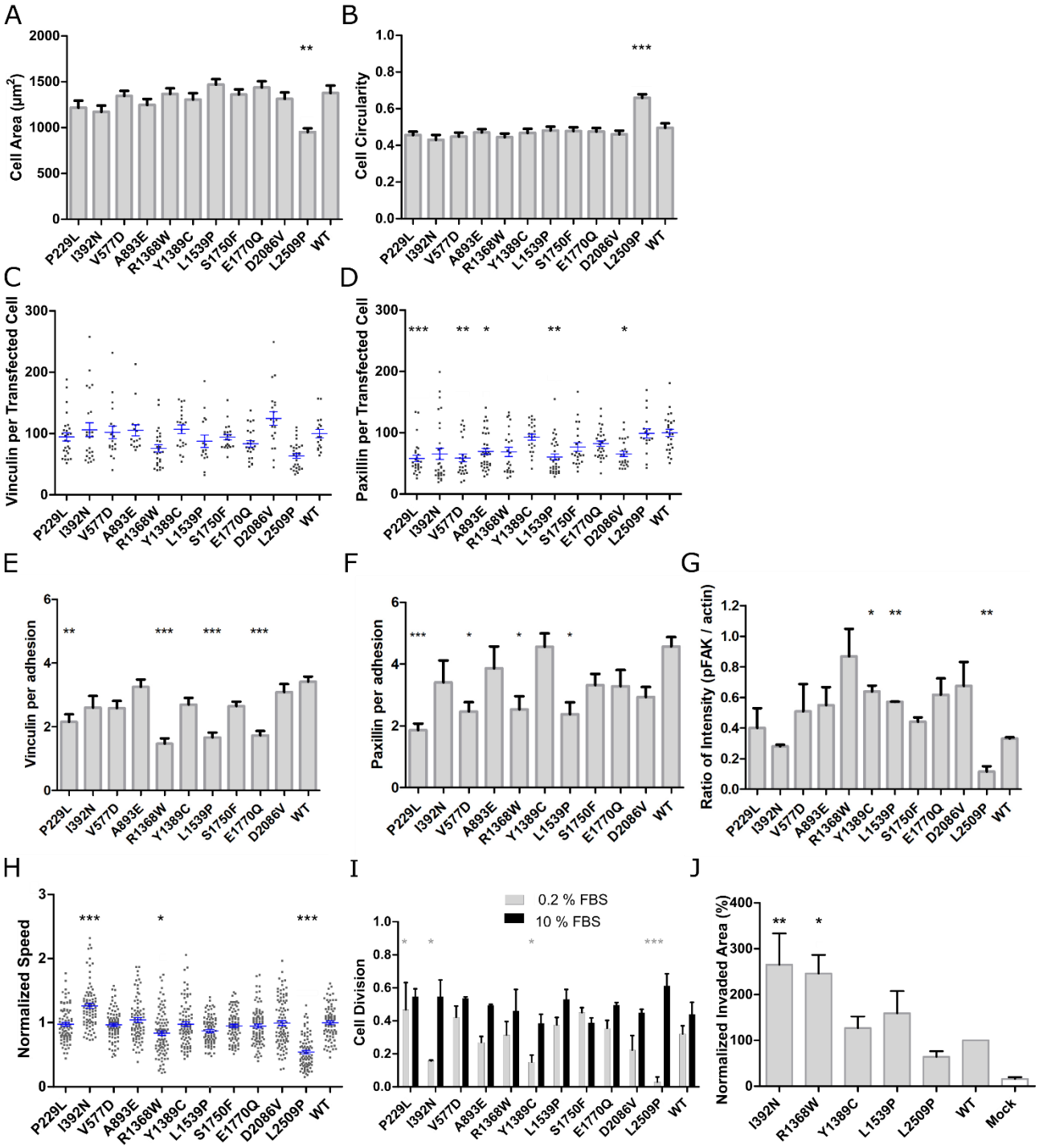

Figure 2: Talin mutations affect cell morphology, cell migration, polarity and FA composition. A, B) Cell area (A) and circularity (B) were quantified from microscopy images of cells expressing the transiently transfected talin-1 point mutant constructs; n~40 cells per mutation pooled from four separate experiments. C, D) Total expression levels of immunolabelled vinculin (C), and paxillin (D) quantified from talin expressing cells; n~30 cells per mutation pooled from two separate experiments for each analysis. E, F) Analysis of vinculin (E) and paxillin (F) colocalisation with talin in adhesions; n~20 cells per mutation from two separate experiments. G) FAKpTyr397 expression levels quantified from two western blots. The statistical analysis was calculated by unpaired t-test. (H) Random migration speed (µm/min) determined from time-lapse images of talin expressing cells. I) Cell proliferation analysis in the presence of 10% FBS and 0.2% FBS, showing the number of times the cells divide in 12 h; n~80 cells per mutation from four separate experiments. The statistical analysis was calculated by t-test, non-parametric test of Mann-Whitney: *P<0.05, **P<0.01, ***P<0.001 compared to WT for each condition. J) Invasion assay through Matrigel matrix towards 10% FBS containing medium. Control cells were mock-transfected with GFP-expressing plasmid. The values are normalised to WT and statistical significance measured in comparison to WT. Data are mean +/-SEM. The statistical significance was analysed by one-way ANOVA and Bonferroni test (or t-test in C and H): *P<0.05, **P<0.01, ***P<0.001.

Cancer-derived talin-1 point mutations affect adhesion composition and promote cell invasion and proliferation

To study the functional characteristics of the talin mutants, we measured random cell migration speed on fibronectin-coated coverslips (Fig.2H). WT-transfected cells had an average migration speed of 0.65 µm/min. I392N was the only mutant that caused increased migration speed (0.82 µm/min). In contrast, the mutations R1368W and L2509P showed a significant decrease in cell migration with average speeds of 0.54 and 0.37 µm/min, respectively. Cells expressing L1539P showed slightly slower migration rate compared to WT expressing cells.

In full-serum conditions the mutants (Fig.2I) and the mock-transfected cells (Fig.S2C) showed equally efficient cell division when compared to the WT talin-1 expressing cells. However, during serum depletion, I392N, Y1389C and mock-transfected cells showed significant decrease (95%, 71% and 47%) and the P229L showed slight increase in cell division (Figs. 2J and S2C) as compared to the cells transfected with WT talin-1, suggesting that talin-1 mediated changes can affect cell proliferation.

Based on the migration and cell proliferation data, we selected I392N, R1368W, Y1389C, L1539P and L2509P for invasion assays and further analysis. We characterised how these five mutants affected the ability of cells to invade through a 3D Matrigel matrix. The mutants I392N and R1368W showed the highest invasion rates, whereas Y1389C, L1539P and L2509P did not significantly differ from WT. Further, the mutant L2509P, which showed a poorly polarised cell phenotype (Fig.2A,B) and significantly reduced migration speed on 2D culture (Fig.2H), was only able to promote limited cell invasion in 3D (Fig.2J).

The I392N mutation in F3 affects talin head stability and promotes invasion

I392 is located inside the hydrophobic core of the F3 subdomain (Fig.3B,C). Mutation of Isoleucine to Asparagine (I392N) leads to replacement of the highly hydrophobic side chain with a hydrophilic side chain. An F3 I392N mutant was insoluble precluding biochemical analysis. Therefore, we explored the functional impact of I392N with the aid of molecular dynamics (MD) simulations. MD simulation predicted that F3 fold is destabilised by the mutation as water molecules may penetrate inside (Fig.3D,E). Alchemical calculations of free energy changes in protein stability upon the mutation showed severe destabilisation of talin head by 38.28 ± 1.27 kJ/mol.

The mutation is in close proximity to the integrin binding site in F3, (PDB:2H7D (Wegener et al., 2007)), so might affect integrin binding and alter talin-dependent integrin activation. Immunofluorescence analysis of the cells transfected with talin wildtype and I392N mutation were analysed for the localisation of FA components paxillin, FAKpY397 and actin (Fig.3F,G,H) but did not reveal significant changes in their accumulation to adhesion sites as compared to cells expressing WT talin.

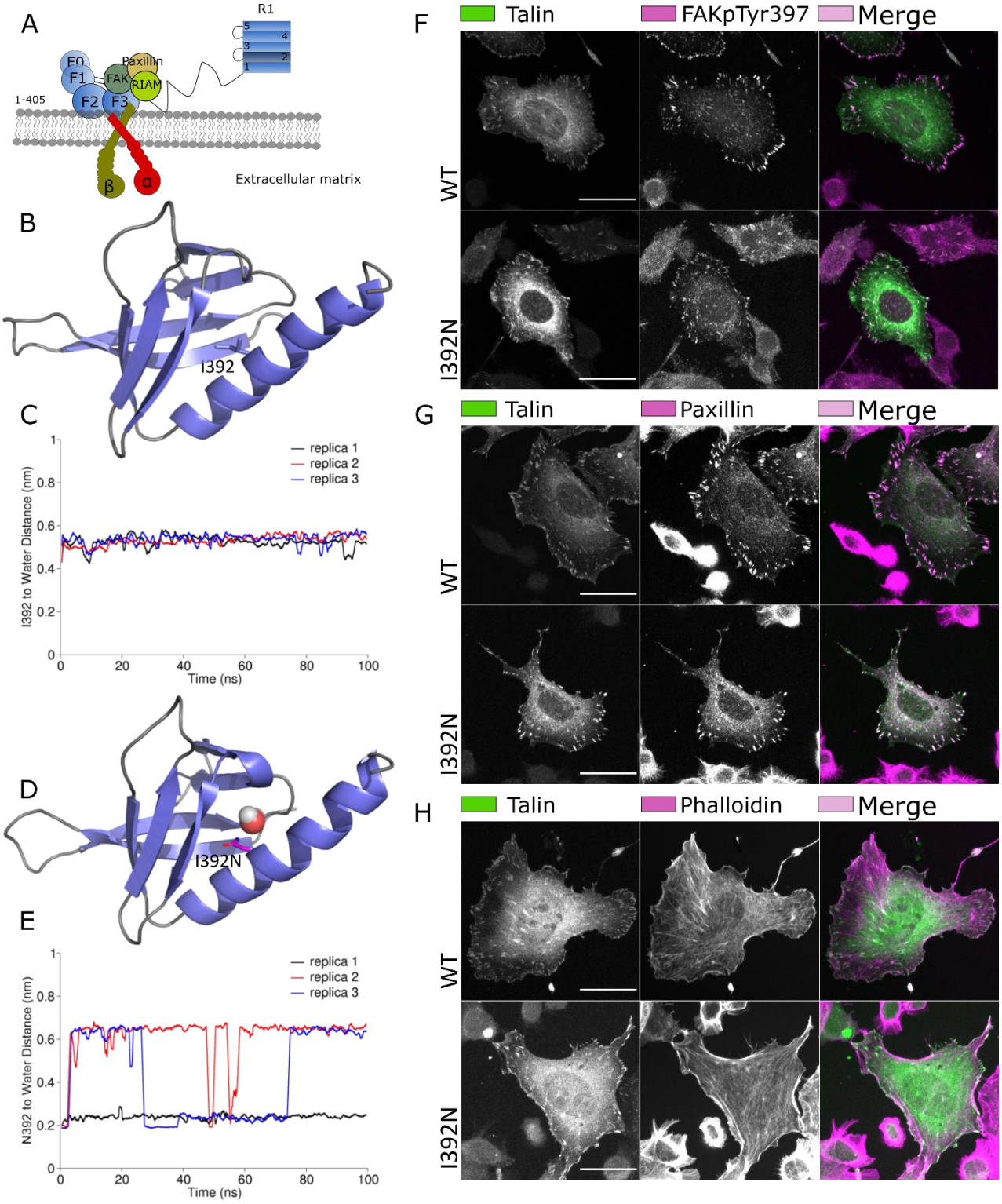

Figure 3: Isoleucine to Asparagine mutation at position 392 destabilises the F3 subdomain. A) Cartoon of the talin head domain and its binding partners. B, C, D, E) Structure snapshots of the F3 subdomain captured at 100 ns of the MD simulation for WT (B) and I392N mutant (D). Residue 392 and a water molecule inside the F3 domain in the I392N mutant simulation are shown (D). The distance between the residue 392 side chain and closest water molecule as function of the MD simulation time in WT (C) and I392N (E) mutant. Three 100-ns simulations are shown. The distance of ~0.6 nm in the WT indicates that the closest water molecule is located at the F3 surface, while in the I392N mutant the distance ~0.2 nm indicates that the water molecule penetrated the F3 fold. F, G, H) SUM projections of z-stacks of talin-1 transfected cells immunolabelled with focal adhesion markers FAKpTyr397 (F), paxillin (G) and actin visualised using phalloidin (H). Scale bars are 25 µm.

Mutations decrease the stability of R7-R8 and affect vinculin binding, leading to increased invasiveness

To investigate how the mutations R1368W, Y1389C and L1539P affect the overall conformation of R7-R8 fragment, MD simulations were performed. Intriguingly, over the course of 100 ns MD, we observed formation of a transient interaction between the R7 and R8 domains in the R1368W (Fig.S3A). Analysis of the R7–R8 binding free energy using the Molecular Mechanics Poisson-Boltzmann Surface area (MM-PBSA) method suggested that the R1368W mutation may enhance an interaction between R7 and R8 (Fig.4B, Fig.S3A). However, the peak dispersion in NMR remained mostly the same with uniform intensity in both spectra, suggesting that R1368W does not significantly modulate talin structure (Fig.S3B). In addition, circular dichroism (CD) analysis of the R7-R8 R1368W and WT yielded similar spectra, showing no change in thermal stability which supports the NMR analysis (Fig.4C).

In contrast, the NMR spectra of R7-R8 Y1389C showed drastic changes in peak positions and loss of peak dispersion indicative of a less well folded form compared to the wildtype (Fig.S3C). Mutation to cysteine introduces the possibility of a potential to form a disulphide bond. To test whether the effects seen are due to disulphide bond formation with the adjacent cysteine (C1392), we performed this analysis in the presence and absence of dithiothreitol and saw no difference between the spectra. Interestingly, the Y1389C mutation caused a striking 6.5°C reduction in the thermostability of R7-R8 (45.5°C compared with 52°C for the wildtype) assessed using CD (Fig.4C). MD simulations carried out for Y1389C and WT in R7-R8 did not reveal significant structural arrangement of the domains, in line with CD spectroscopy analysis which showed no observable changes in the helicity of the proteins.

Talin can reveal a number of cryptic VBS along the rod domain, two of which are located in the R7-R8 region, and are regulated by stability of the α-helical bundles in response to mechanical load (del Rio et al., 2009;Gingras et al., 2005;Hytonen and Vogel, 2008). To determine whether vinculin Vd1 domain (residues 1-258) binding to talin was affected by the R1368W and Y1389C mutations we used a size exclusion chromatography assay as previously described (Gingras et al., 2010). Our previous study showed that despite containing two VBS, only one of them is accessible to vinculin (Gingras et al., 2010), and here we found that R7-R8 WT and R1368W both only bind one vinculin Vd1 molecule (Fig.4E). In contrast, the Y1389C mutation, which is in the core of the R7 domain (Fig.4D), can bind two Vd1 molecules, indicating that this mutation enhances the accessibility of the R7 vinculin binding site (Fig.4E) and alters the stoichiometry of the R7-R8:vinculin interaction.

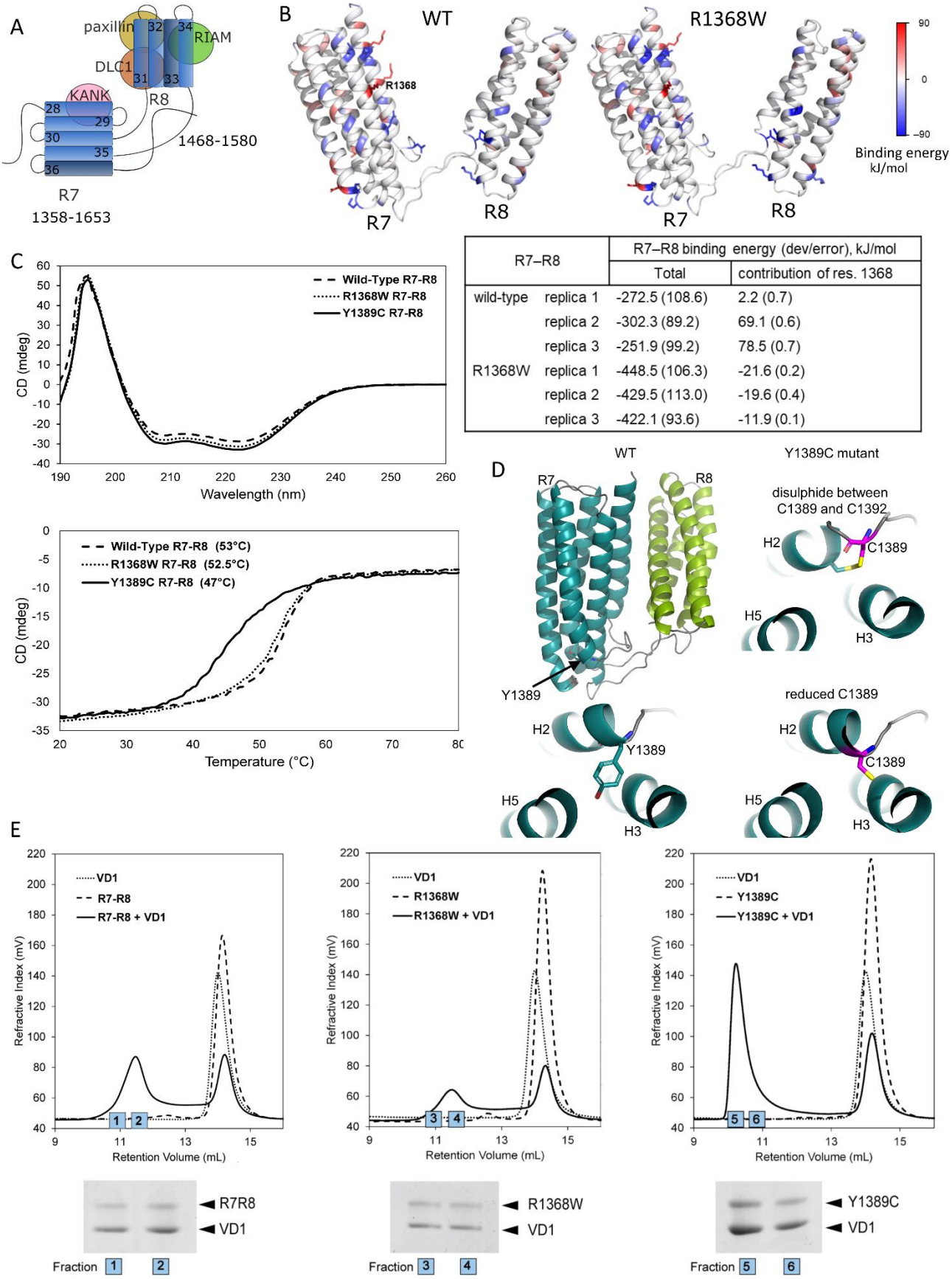

R7–R8		R7–R8 binding energy (dev/error), kJ/mol	
		Total	contribution of res. 1368
wild-type	replica 1	-272.5 (108.6)	2.2 (0.7)
	replica 2	-302.3 (89.2)	69.1 (0.6)
	replica 3	-251.9 (99.2)	78.5 (0.7)
R1368W	replica 1	-448.5 (106.3)	-21.6 (0.2)
	replica 2	-429.5 (113.0)	-19.6 (0.4)
	replica 3	-422.1 (93.6)	-11.9 (0.1)

Figure 4. Influence of point mutations in R7-R8 domains on biophysical properties of talin. (A) Cartoon of the R7-R8 domains and binding partners. (B) Inter-domain binding energy for R7-R8 WT and R1368W using MM-PBSA for

every 250 ps snapshot of the MD trajectory. Data in the table shows that the total inter-domain binding energy in R1368W mutant is higher than for WT. (C) Melting temperature curves for R7-R8 WT, R1368W and Y1389C measured using CD spectroscopy. (D) Structure snapshots captured at 100 ns of MD for R7-R8 WT (left) and Y1389C (right). (E) Vinculin Vd1 binding analysed by size exclusion chromatography for R7-R8 WT (left), R1368W (centre) and Y1389C (right).

MD simulations revealed that the L1539P mutation effectively breaks the structure of helix three (H3) in the R8 subdomain (Fig.S4C), and secondary structure analysis using DSSP indicated clear disruption of H3 in the L1539P-mutated R8 when compared to wildtype (Fig.S4D). Furthermore, CD analysis demonstrated a reduction in thermostability of the R7-R8 L1539P mutant by 3.5°C and reduced secondary structure composition (Fig.S4E). Immunostaining showed the L1539P mutation had lower vinculin recruitment to focal adhesions (Fig.2E), suggesting that disrupting H3 might affect vinculin binding. No changes in DLC1 localisation were observed (Fig.S5), even though the DLC1 binding site is in R8, adjacent to the mutation (Guorong Li et al., 2011;Zacharchenko et al., 2016).

A Fluorescence Polarisation (FP) assay was used to determine the impact of these mutations on ligand binding to R7 and R8. Neither KANK1 binding to R7 nor RIAM binding to R8 had significant differences in binding affinity with the R1368W and Y1389C mutants as compared to WT (Fig.S4A,B). The talin-KANK1 interaction is important for coordinating the targeting of microtubules to adhesion sites (Bouchet et al., 2016). Consistent with the negligible impact on the talin-KANK1 interaction no apparent changes in tubulin organisation between WT, R1368W, Y1389C, and L1539P R7-R8 were observed (Fig.S3D, Fig.S5). Together, this analysis points to the increased invasiveness of these mutants being a result of altered domain stability and altered accessibility of the VBS.

L2509P breaks talin dimerisation, inhibiting polarisation and migration in 2D

Talin-deficient fibroblasts transfected with L2509P mutant showed drastic changes in cell phenotype and notably slower (57%) random cell migration when compared to WT-expressing cells (Fig.2H). As the mutation is situated in the dimerisation domain (DD) which forms part of the C-terminal actin binding site 3 (Gingras et al., 2008) , we set out to explore the effects of the mutation on dimerisation and actin interactions in more detail. We engineered truncated talin-1 constructs with deletions in the c-terminus as follows: WT (residues 1-2541), ΔDD (residues 1-2493), ΔR13-DD (residues 1-2299) and ΔR1-DD (residues 1-481) (Fig.5B). Immunofluorescence analysis of the cells transfected with L2509P, ΔDD, ΔR13-DD and ΔR1-DD showed loss of; i) maturation of adhesion, ii) localisation of the FA components and iii) filamentous actin into the adhesion sites, indicating that the point mutation L2509P disrupts dimerisation and interaction with actin. Furthermore, all of the constructs led to

anisotropic cell spreading (Fig.5C) as observed earlier for cells expressing talin head alone (Rahikainen et al., 2019).

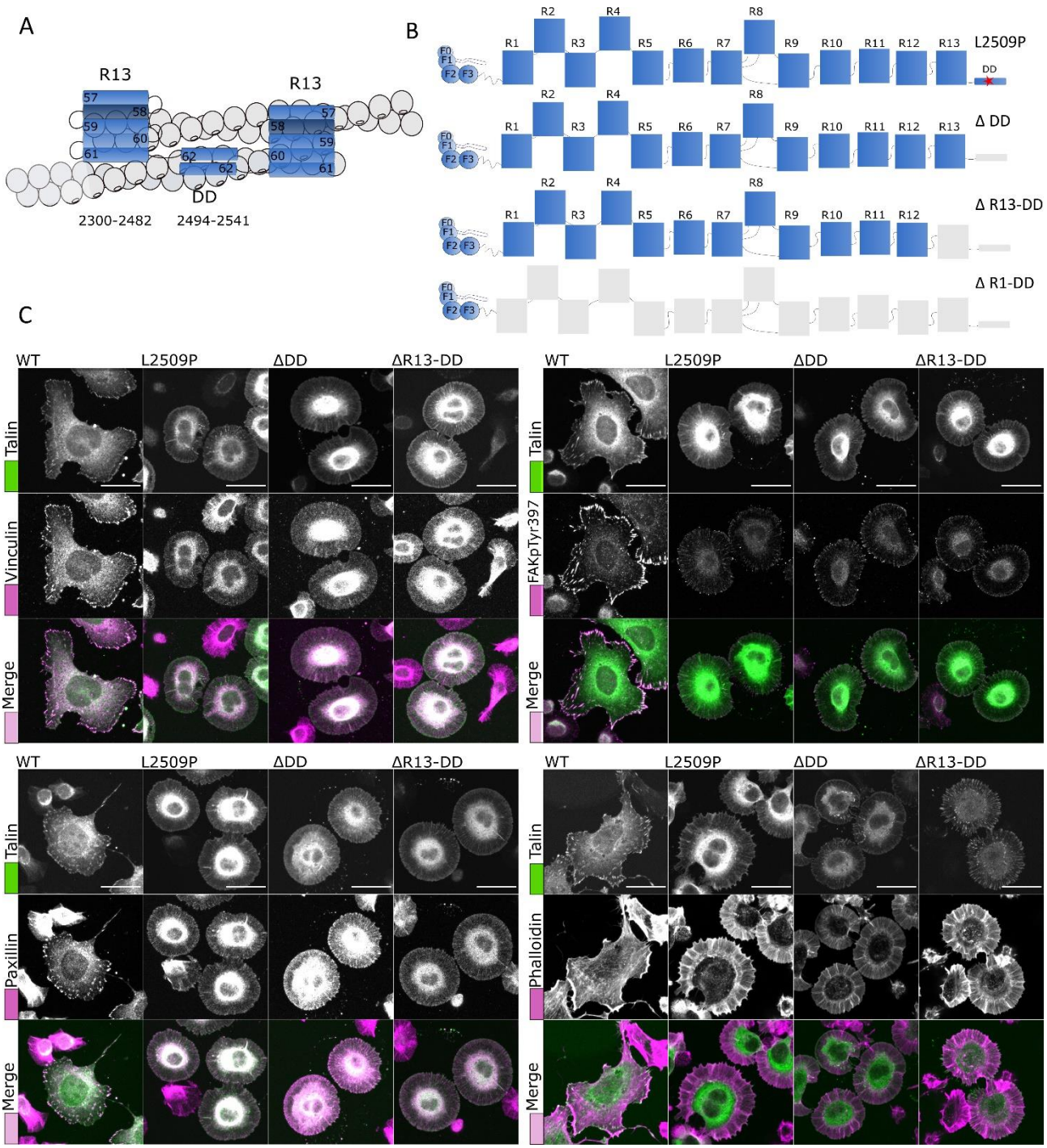

Figure 5: All talin DD mutants showed a loss of co-localisation with FA markers. A) Cartoon of the R13-DD dimerisation domain bound to actin. B) Schematic representation of the point mutation L2509P in full length talin and the truncations; ΔDD, ΔR13-DD and ΔR1-DD. C) SUM projections of z-stacks of cells expressing WT, L2509P, ΔDD, ΔR13-DD talin and immunolabeled against vinculin, FAKpTyr397 and paxillin. Fluorochrome-conjugated phalloidin was used to visualise actin filaments. No clear localisation of any of the FA components was evident with any of the mutants. Scale bars are 25 µm.

MD simulations revealed high flexibility of the mutated helix as the proline in the mutant form, breaks the helix structure (Fig.6A). This disruption of the coiled coil is expected to affect the dimerisation of talin and thus actin binding. Size exclusion chromatography showed that wildtype R13-DD (residues 2300-2541) is a constitutive dimer consistent with our previous study (Gingras et al., 2008). In contrast the L2509P mutant of the R13-DD runs as a monomer, confirming that the proline is breaking the helix and disrupting talin dimerisation (Fig.6B). The impact on cell migration, invasion, area and circularity was the same for the L2509P and the truncated mutants whether we removed the entire rod, R13-DD, DD or applied the point mutation L2509P (Fig.6C,D,E,F).

Since many cell types express both, talin-1 and talin-2, we were curious to see if L2509P could have a dominant effect over talin-2. Indeed, we found that migration speed decreased significantly for talin-1 L2509P even in the presence of talin-2 when compared to cells co-transfected with both WT talins or as compared to cells expressing talin-2 alone (Fig.6G).

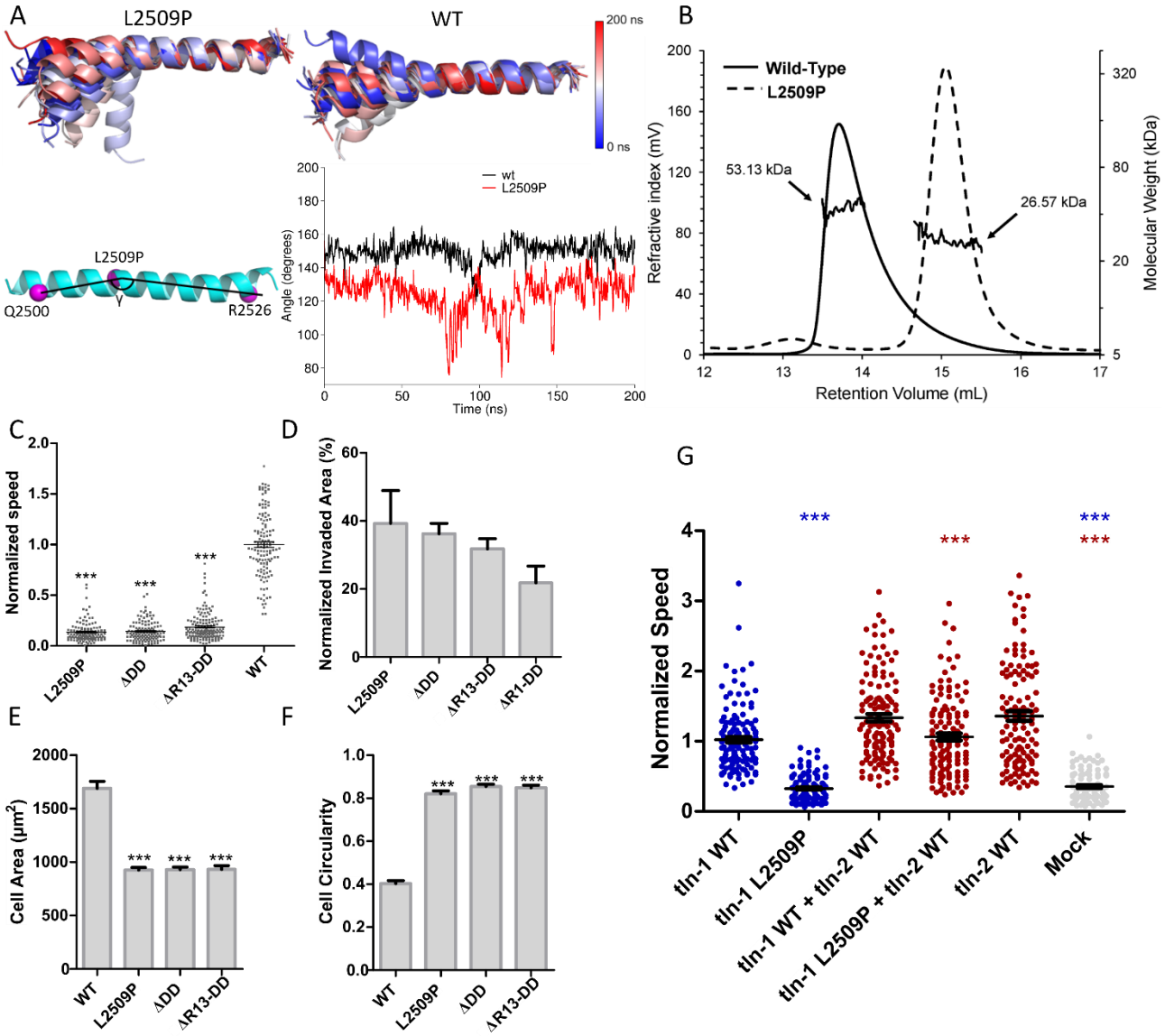

Figure 6: The L2509P mutant severely impacts talin function. A) MD simulation of DD helix showing high flexibility of the helix caused by L2509P compared to the WT. Superposition was performed using C-alpha atoms of residues 2510 to 2529. The angle (γ) in L2509P mutant and WT DD in single helix measured as a function of time. B) SEC-MALS analysis of R13-DD WT and L2509P showing that the R13-DD L2509P is monomeric. C) Migration speed on 2D surface showing reduced migration speed in all mutated/truncated constructs in comparison to WT. D) Cell invasion through Matrigel in 3D environment showing the invasiveness potential of the L2509P and truncated talin constructs. Invasion assay was repeated at least three times in triplicate chamber for each construct. E, F) Cell area (E) and cell circularity (F) analysis showing decreased cell surface area and reduced polarisation of the mutated/truncated constructs compared to WT; n~70 cells from three separate experiment. Data is normalised to WT (WT = 100%). Data are mean +/-SEM. The statistical significance of all results analysed by one-way ANOVA and Bonferroni test: *P<0.05, **P<0.01, ***P<0.001. G) Migration assay on 2D surface showing reduced migration speed in the cells co-transfected with talin-1 L2509P and full-length WT talin-2. The statistical significance of all results analysed by one-way ANOVA and Bonferroni test: *P<0.05, **P<0.01, ***P<0.001. The results are normalised with only WT talin-1 (blue) or WT talin-1+ WT talin-2 (red).

Discussion

Talin is a central regulator of cell adhesion to the ECM and is critical for integrin activation and FA formation. It provides mechanical linkage between ECM and actin cytoskeleton, and is an essential scaffold for the organisation of the FA multi-protein complex (Zhang et al., 2008). Loss of anchorage-dependent growth, changes in ECM remodelling, and cytoskeletal changes are necessary for cancer progression (Jaalouk and Lammerding, 2009). There are two isoforms of talin, talin-1 and talin-2, which show different expression patterns. While talin-1 is expressed in all tissues, talin-2 has more variability and overall lower expression levels. Overall expression levels, derived from GEPIA gene expression server (Tang et al., 2017), indicate that talin-1 expression levels show more variance between different cancers and their counterpart healthy tissues than those of talin-2. Due to the more ubiquitous nature of talin-1 (Fig.7), we only assess the talin-1 mutations here. Several cancer types show significant changes in talin-1 expression level. The highest overexpression is associated with Glioblastomas (GBM; >300%), Brain Gliomas (LGG; >300%) and Pancreatic adenocarcinomas (PAAD; >300%). In contrast, the most drastic talin-1 downregulation is seen in uveal melanoma (UCS; -25%) and endometrial carcinoma of the uterine (UCEC; -25%) (Fig.7).

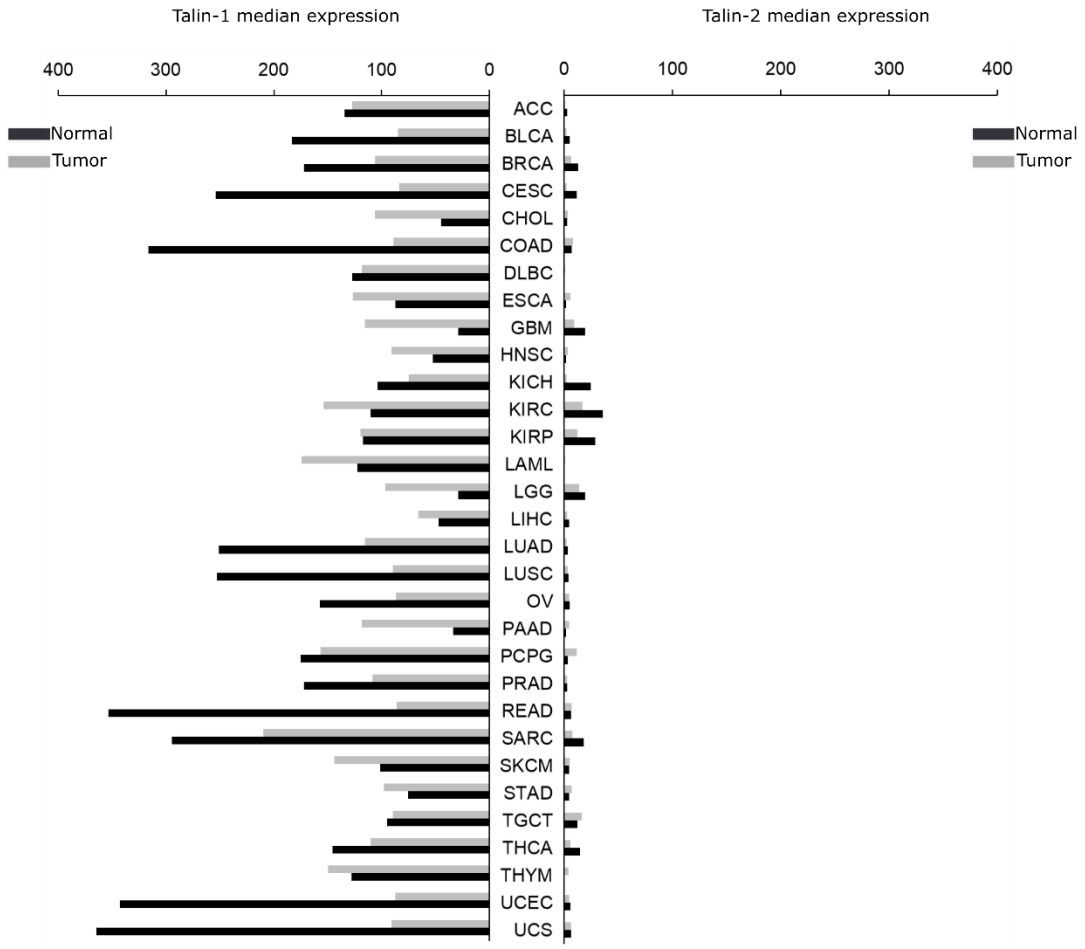

ACC Adrenocortical carcinoma
BLCA Bladder Urothelial Carcinoma
BRCA Breast invasive carcinoma
CESC Cervical squamous cell carcinoma and endocervical adenocarcinoma
CHOL Cholangiocarcinoma
COAD Colon adenocarcinoma
DLBC Lymphoid Neoplasm Diffuse Large B-cell Lymphoma
ESCA Esophageal carcinoma
GBM Glioblastoma multiforme
HNSC Head and Neck squamous cell carcinoma
KICH Kidney Chromophobe
KIRC Kidney renal clear cell carcinoma
KIRP Kidney renal papillary cell carcinoma
LAML Acute Myeloid Leukemia
LGG Brain Lower Grade Glioma
LIHC Liver hepatocellular carcinoma
LUAD Lung adenocarcinoma
LUSC Lung squamous cell carcinoma
MESO Mesothelioma
OV Ovarian serous cystadenocarcinoma
PAAD Pancreatic adenocarcinoma
PCPG Pheochromocytoma and Paraganglioma
PRAD Prostate adenocarcinoma
READ Rectum adenocarcinoma
SARC Sarcoma
SKCM Skin Cutaneous Melanoma
STAD Stomach adenocarcinoma
TGCT Testicular Germ Cell Tumours
THCA Thyroid carcinoma
THYM Thymoma
UCEC Uterine Corpus Endometrial Carcinoma
UCS Uterine Carcinosarcoma
UVM Uveal Melanoma

Figure 7: Talin-1 and talin-2 gene expression profiles across tumour and paired normal samples. Expression levels taken from GEPIA database, at the time of analysis GEPIA contained 9662 tumour and 5540 normal samples across 33 cancer types.

With the aid of biochemical analyses, molecular modelling and functional cell biology assays, we found that mutations in talin-1 affect cellular processes linked with cancer progression, such as migration, invasion and proliferation. We have shown previously that the mechanical stability of the talin rod alpha-helix bundles can be drastically influenced by point mutations and these small changes can further lead into changes in traction forces and cellular response (Goult,Zacharchenko et al., 2013;Han et al., 2019;Rahikainen et al., 2017). Furthermore, point mutations in talin can have dramatic effects on cell behaviour (Gingras et al., 2008;Goult,Xu et al., 2013;Rahikainen et al., 2017).

Out of the eleven mutants studied here, I392N, originally found from pancreatic carcinoma, had the most pronounced effect in terms of activating migration and invasion. However, this mutation also showed lower talin expression levels when compared to WT and other mutants transfected similarly (Fig.S1A) suggesting that the mutation could affect talin stability and expression levels.

The R7-R8 domains have cooperative function, with R8 sitting outside the force transduction pathway, and protected from mechanical stress by R7 (Yao et al., 2016). In addition, there are binding sites for multiple molecules such as KANK, DLC1, RIAM, paxillin and vinculin in both domains. We found that random migration on 2D and invasion through Matrigel, were significantly affected by the mutation R1368W (Fig.2H,J). MD simulation suggested that the R1368W mutant might enhance interactions between R7 and R8 domains (Fig.4B), which might perturb the localisation of the FA markers within adhesion (Fig.2E,F) affecting cell behaviour. However, binding affinity for KANK and protein stability remained consistent with WT, suggesting that the cellular effects of this mutation could be due to an, as of yet, unidentified R7 function perturbed in this mutant.

One of the interesting findings was the effect the Y1389C mutation in R7 had on vinculin binding. The VBS in R7 is one of the hardest to expose (Gingras et al., 2010) but can be stretch activated (Yao et al., 2016), however, the Y1389C mutation significantly enhanced the VBS accessibility (Fig.4E). Gel filtration analysis of vinculin Vd1 binding to Y1389C revealed that while R7-R8 WT and the R1368W mutant only bind a single Vd1 molecule, the R7-R8 Y1389C was able to bind two Vd1 (Fig.4E). This suggests that introduction of the mutation destabilises the R7 helical bundle, allowing vinculin binding more readily in the absence of force. Furthermore, reduced R7 stability will likely have a knock-on effect on R8 stability which may indirectly lead to signalling defects by perturbing R8 (Haining et al., 2018). Interestingly, the destabilisation of R7 did not impact on KANK binding nor cause changes in microtubule network but it did result in enhanced migration and proliferation. The additional actin recruitment via vinculin could have a direct effect on FA dynamics by facilitating formation of talin-vinculin pre-complexes, necessary to enable efficient adhesion maturation (Han et al., 2019). This could also affect actomyosin contractility and Rho/ROCK signalling, which have been shown to regulate cell proliferation (Kumper et al., 2016). Enhanced adhesion maturation was also suggested by the increased pFAK397 levels seen with this mutant.

The most striking phenotype was seen in cells expressing talin mutant L2509P. These cells were unpolarised, small, lacking mature FAs, and showed complete loss of random migratory behaviour. This mutation sits in the talin dimerisation domain, a single helix which forms an antiparallel dimer.

Interestingly, the same phenotype was observed with complete removal of the dimerisation domain helix (ΔDD) as with L2509P point mutation. Size exclusion chromatography with multi-angle light scattering (SEC-MALS) analysis of the wildtype R13-DD showed a constitutive dimer in solution whilst the L2509P mutant resulted in complete loss of dimerisation (Fig.6B). We also detected that overexpression of vinculin in L2509P transfected cells led to the polarisation of cells (data not shown), consistent with our previous findings that stabilising the talin link to actin via vinculin can rescue the phenotype (Rahikainen et al., 2019).

Focal adhesion dynamics affect cell proliferation by regulating YAP activation and Hippo pathway, which are balanced between negative signals such as contact inhibition and promoting mitogenic signalling such as growth factors and hormones. Cell shape and mechanotransduction are known to regulate YAP activity, as stretched cells on stiff ECM positively regulate YAP nuclear localisation (Dupont et al., 2011). This regulation is believed to be independent of the canonical Hippo-pathway or cell-cell junctions but mediated by Rho-ROCK signalling and actin dynamics (Gumbiner and Kim, 2014). However, cell adhesion to fibronectin, but not poly-D-lysine or laminin, can promote YAP translocation via the canonical Hippo pathway, suggesting that adhesion-mediated integrin activation can mimic mitogen-caused activation, without the presence of soluble mitogenic growth factors (Kim and Gumbiner, 2015). This possibly explains the rescue of cell proliferation of mock-transfected cells in serum-free conditions by talin expression. Interestingly, mutants I392N, Y1389C and L2509P all decreased proliferation in low-serum conditions with I392N showing increased migration and L2509P decreased migration further highlighting the complexity of the signalling. The exact signalling pathways affected by these talin mutations would be interesting targets for further studies.

In this study, we explored hundreds of talin-associated mutations and selected 11 mutants for thorough analysis. Out of those, two mutants promoted cell invasion, one mutant significantly accelerated cell migration in 2D and eight mutants enhanced cell proliferation. The contribution of talin to cancer progression is timely. During this study, ~200 more cancer-associated talin mutations have been added to the COSMIC database and there are recent studies discussing the connection between talin and cancer (Huang et al., 2020;Malla and Vempati, 2020). The work we present here demonstrates how single point mutations in talin can drastically alter cell behaviour, potentially contributing to cancer metastasis.

Materials and methods

Cell lines and talin constructs

Theodosiou et al. (Theodosiou et al., 2016) previously described the TLN1$^{-/-}$TLN2$^{-/-}$ mouse embryonic fibroblast (MEF) cell line. Cells were maintained in a humidified 37°C, 5% CO_2 incubator. High glucose Dulbecco´s modified Eagle medium (DMEM) supplemented with 10% fetal bovine serum (FBS) was used in all experiments except in the starvation conditions where 0.2% serum was used. The cell line was regularly tested for mycoplasma contamination. Talin variants were subcloned into a modified pEGFP-C1 vector backbone (Clontech). Cells were transfected with 6 µg plasmid DNA per 10^6 cells using Neon transfection system (Thermo Fisher Scientific) using parameters 1400 V, 30 ms, one pulse. The expression constructs for cell culture experiments with the c-terminal EGFP-tag are as follows: wild-type talin-1 1-2541; ΔR13-DD (1-2299); ΔDD (1-2493); ΔR1-DD (1-481) and the point mutants in the full length talin-1 P229L, I392N, V557D, A893E, R1368W, Y1389C, L1539P, S1750F, E1770Q, D2086V, L2509P.

Migration and Matrigel invasion analysis

Transfected cells were incubated for 24 h, trypsinized and plated on the well-plates coated with 10 µg/ml fibronectin. Cells were allowed to attach for 90 minutes, after which the medium was changed. The time-lapse images captured with EVOS FL auto microscope (Thermo Fisher Scientific) were analysed manually using ImageJ (Fiji) and MTrackJ plugin (Meijering et al., 2011;Schneider et al., 2012).

Corning BioCoat Matrigel Invasion Chamber containing an 8-micron pore size PET membrane with a thin layer of Matrigel basement membrane matrix were used for the invasion assay. Transfected TLN1$^{-/-}$TLN2$^{-/-}$ MEF cells were cultured overnight, followed by cultivation in starvation medium containing 0.2% FBS for 40-45 h. Number of transfected cells was measured by Luna-FL dual Fluorescence Cell Counter (BioCat GmbH) Chambers prepared according to the manufacturer. DMEM medium containing 10% FBS was used as chemoattractant in the lower level of chamber. The chamber plate was incubated at humidified 37°C and 5% CO_2 incubator for 24 h, after which the cells were fixed with 100% methanol. Cells were stained with 0.2% crystal blue for 10 minutes following by rinsing the excess stain. The non-invaded cells were removed from the upper membrane surface using cotton tipped swab. The inserts were allowed to air dry overnight. The membrane was removed using scalpel and placed bottom side down on a microscope objective slide on which a small drop of immersion oil. The membranes were scanned using PRIOR OpenStand microscope using 20x

objective and Jilab SlideStrider software (1.2.0). The invaded cell area was calculated using ImageJ (Fiji). Invasion assay was repeated at least three times in triplicate chamber for each selected construct.

Immunostaining and confocal imaging

After 24 h transfection, cells were trypsinized and plated on coverslips coated with 10 µg/ml fibronectin and incubated for 24 h. Cells were fixed with 4% paraformaldehyde, permeabilised and immunostained using standard protocol. Antibodies are listed in Table S1.

Immunostained samples were imaged with Zeiss Cell ObserverZ1 inverted microscope and LSM 780 confocal unit (Zeiss, Oberkochen, Germany) using 63x/1.4, WD 0.19 mm oil immersion objective. Images were taken using Zeiss Zen Black software and analysed by ImageJ as described previously (Rahikainen et al., 2019). Within each experiment, the imaging parameters were kept constant to allow quantitative image analysis. Detailed image analysis is described in Supplementary material.

Western blotting

Transfected cells were grown for 24 h, lysed with RIPA buffer supplemented with protease inhibitor cocktail (Sigma-Aldrich lot#126M4016V). After centrifugation, cell lysates were applied on an SDS-PAGE to separate protein. A wet blot system was used to transfer the separated protein from gel onto a polyvinylidene fluoride (PVDF) membrane. Blots were quantified using ImageJ. Antibodies are listed in Table S1.

Constructs for protein expression in *E. coli*

The talin-1 fragments, generated using full-length talin-1 as a template, were introduced into a modified pHis vector to create N-terminal His6-tag constructs. The His6-tag is separated from talin fragment by an eleven-residue linker: SSSGPSASGTG. Mutagenesis was performed using QuikChange II Site-Directed Mutagenesis kit. Talin constructs were expressed in BL21(DE3) *E. coli* cells and induced with 0.1 mM IPTG at 18°C for overnight. Clarified lysates were loaded onto an affinity column (HisTrap HP 5 ml; GE Healthcare). Eluted protein was further purified using anion exchange column (HiTrap Q HP 5 ml; GE Healthcare) before buffer exchange into PBS and stored at -20°C.

NMR Spectroscopy and Fluorescence Polarisation Assay

Talin constructs were grown in 2M9 minimal media with ^{15}N-labelled NH_4Cl. Protein was purified as above and buffer exchanged into 20 mM Na-phosphate pH 6.5, 50 mM NaCl, 2 mM DTT, 5% (v/v) D_2O. NMR spectra were obtained at 298 K on a Bruker AVANCE III 600 MHz spectrometer equipped with CryoProbe. All R7-R8 ^{1}H,^{15}N-HSQC spectra were obtained at a concentration of 160 µM. For fluorescence polarisation (FP) experiments, peptides were synthesised by GLBiochem (China) and coupled with either BODIPY or Fluorescein dye via a C-terminal cysteine residue.

Size Exclusion Chromatography with Multi-Angle Light Scattering

Talin R13-DD wild-type and L2509P were analysed by SEC-MALS at a concentration of 100 µM at room temperature with a Superdex 75 column (GE Healthcare Life Sciences). Eluted proteins were analysed with Viscotek SEC-MALS 9 and Viscotek RI detector VE3580 (Malvern Panalytical). Molecular mass was determined using OmniSEC software. For analysis of Vd1 binding to talin, proteins were incubated at a 1:1 ratio at a concentration of 100 µM and analysed at room temperature.

MD Simulations

RCSB PDB structures were used as starting conformations for MD: 2H7E for F3 (Wegener et al., 2007), 2X0C for R7-R8 (Gingras et al., 2010) and 2QDQ for DD domain (Gingras et al., 2008). The R7-R8 binding energy was calculated using MM-PBSA (Kumari et al., 2014). Structural analysis was performed using PyMOL and VMD (Humphrey et al., 1996). MD simulations were performed using Gromacs (Abraham et al., 2015) at the Sisu supercomputer, CSC, Finland. The CHARMM27 force field (MacKerell et al., 1998) and explicit TIP3P water model (Jorgensen and Madura, 1983) in 0.15 M KCl solution were used. The energy minimisation of the system was performed in 10000 steps. The system was equilibrated in three phases using harmonic position restraints on all heavy atoms of the protein. Integration time step of 2 fs was used in all the simulations. NPT ensemble was maintained at 310 K using the V-rescale algorithm (Bussi et al., 2007), and 1 atm using Berendsen algorithm (Berendsen et al., 1984). Alchemical free energy calculations were prepared using PMX (Gapsys et al., 2015). The simulations were performed using Amber99SB*-ILDN force field (Lindorff-Larsen et al., 2010) and TIP3P water model in 0.15 M NaCl solution, following standard procedure. The whole calculation was repeated three times and average free energy value was obtained.

Acknowledgements

This research was supported by the Academy of Finland (grant 290506 to V.P.H. and grant 323021 to V.V.M.), a Biotechnology and Biological Sciences Research Council grant BB/N007336/1 (B.T.G.) and a Human Frontier Science Program grant RGP00001/2016 (B.T.G.). L.A. received support from the graduate school of Tampere University and the Anu Kirra´s grant foundation. We acknowledge CSC for supercomputing resources and Biocentre Finland for infrastructure support. The authors acknowledge the Biocenter Finland (BF) and Tampere Imaging Facility (TIF) for the services. We thank Prof. Reinhard Fässler and Dr Carsten Grashoff (Max Planck Institute of Biochemistry) for help with $Tln^{1-/-}Tln^{2-/-}$ cells; Prof. Michael Sheetz (National University of Singapore) for providing the mouse wild-type talin expression construct. We thank Rolle Rahikainen, Anssi Nurminen and Sampo Kukkurainen (Tampere University) for their support and insights. Ulla Kiiskinen and Niklas Kähkönen (Tampere University) are acknowledged for technical support

Competing interests

The authors declare no competing or financial interests.

References

Abraham, M. J., Murtola, T., Schulz, R., Páll, S., Smith, J. C., Hess, B. and Lindahl, E. (2015). GROMACS: High performance molecular simulations through multi-level parallelism from laptops to supercomputers. *SoftwareX* **1-2,** 19-25.

Anthis, N. J., Wegener, K. L., Ye, F., Kim, C., Goult, B. T., Lowe, E. D., Vakonakis, I., Bate, N., Critchley, D. R., Ginsberg, M. H. et al. (2009). The structure of an integrin/talin complex reveals the basis of inside-out signal transduction. *EMBO J.* **28,** 3623-3632.

Ashkenazy, H., Abadi, S., Martz, E., Chay, O., Mayrose, I., Pupko, T. and Ben-Tal, N. (2016). ConSurf 2016: An improved methodology to estimate and visualize evolutionary conservation in macromolecules. *Nucleic Acids Res.* **44,** 344.

Atherton, P., Stutchbury, B., Wang, D. Y., Jethwa, D., Tsang, R., Meiler-Rodriguez, E., Wang, P., Bate, N., Zent, R., Barsukov, I. L. et al. (2015). Vinculin controls talin engagement with the actomyosin machinery. *Nat. Commun.* **6,** 10038.

Berendsen, H., Postma, J., Vangunsteren, W. F., Dinola, A. and Haak, J. R. (1984). Molecular-dynamics with couplingto an external bath. *Journal of Chemical Physics* **81,** 3684-3690.

Bouchet, B. P., Gough, R. E., Ammon, Y., van de Willige, D., Post, H., Jacquemet, G., Altelaar, A. M., Heck, A. J., Goult, B. T. and Akhmanova, A. (2016). Talin-KANK1 interaction controls the recruitment of cortical microtubule stabilizing complexes to focal adhesions. *eLife* **5,**.

Bussi, G., Parrinello, M. and Donadio, D. (2007). Canonical sampling through velocity rescaling. *Journal of Chemical Physics* **126,** 014101-7.

Chen, P., Lei, L., Wang, J., Zou, X., Zhang, D., Deng, L. and Wu, D. (2017). Downregulation of Talin1 promotes hepatocellular carcinoma progression through activation of the ERK1/2 pathway. *Cancer Science* **108,** 1157-1168.

Clarke, L., Zheng-Bradley, X., Smith, R., Kulesha, E., Xiao, C., Toneva, I., Vaughan, B., Preuss, D., Leinonen, R., Shumway, M. et al. (2012). The 1000 genomes project: Data management and community access. *Nat. Methods* **9,** 459-462.

del Rio, A., Perez-Jimenez, R., Liu, R., Roca-Cusachs, P., Fernandez, J. M. and Sheetz, M. P. (2009). Stretching single talin rod molecules activates vinculin binding. *Science* **323,** 638-641.

Dupont, S., Morsut, L., Aragona, M., Enzo, E., Giulitti, S., Cordenonsi, M., Zanconato, F., Le Digabel, J., Forcato, M., Bicciato, S. et al. (2011). Role of YAP/TAZ in mechanotransduction. *Nature* **474,** 179-183.

Fillingham, I., Gingras, A. R., Papagrigoriou, E., Patel, B., Emsley, J., Critchley, D. R., Roberts, G. C. K. and Barsukov, I. L. (2005). A vinculin binding domain from the talin rod unfolds to form a complex with the vinculin head. *Structure* **13,** 65-74.

Gapsys, V., Michielssens, S., Seeliger, D. and de Groot, B. L. (2015). Pmx: Automated protein structure and topology generation for alchemical perturbations. *J. Comput. Chem.* **36,** 348-354.

Gingras, A. R., Bate, N., Goult, B. T., Hazelwood, L., Canestrelli, I., Grossmann, J. G., Liu, H., Putz, N. S., Roberts, G. C., Volkmann, N. et al. (2008). The structure of the C-terminal actin-binding domain of talin. *EMBO J.* **27,** 458-469.

Gingras, A. R., Bate, N., Goult, B. T., Patel, B., Kopp, P. M., Emsley, J., Barsukov, I. L., Roberts, G. C. and Critchley, D. R. (2010). Central region of talin has a unique fold that binds vinculin and actin. *J. Biol. Chem.* **285,** 29577-29587.

Gingras, A. R., Ziegler, W. H., Frank, R., Barsukov, I. L., Roberts, G. C., Critchley, D. R. and Emsley, J. (2005). Mapping and consensus sequence identification for multiple vinculin binding sites within the talin rod. *J. Biol. Chem.* **280,** 37217-37224.

Goult, B. T., Bate, N., Anthis, N. J., Wegener, K. L., Gingras, A. R., Patel, B., Barsukov, I. L., Campbell, I. D., Roberts, G. C. and Critchley, D. R. (2009). The structure of an interdomain complex that regulates talin activity. *J. Biol. Chem.* **284,** 15097-15106.

Goult, B. T., Xu, X. P., Gingras, A. R., Swift, M., Patel, B., Bate, N., Kopp, P. M., Barsukov, I. L., Critchley, D. R., Volkmann, N. et al. (2013). Structural studies on full-length talin1 reveal a compact auto-inhibited dimer: Implications for talin activation. *J. Struct. Biol.* **184,** 21-32.

Goult, B. T., Yan, J. and Schwartz, M. A. (2018). Talin as a mechanosensitive signaling hub. *J. Cell Biol.* **217,** 3776-3784.

Goult, B. T., Zacharchenko, T., Bate, N., Tsang, R., Hey, F., Gingras, A. R., Elliott, P. R., Roberts, G. C., Ballestrem, C., Critchley, D. R. et al. (2013). RIAM and vinculin binding to talin are mutually exclusive and regulate adhesion assembly and turnover. *J. Biol. Chem.* **288,** 8238-8249.

Gumbiner, B. M. and Kim, N. G. (2014). The hippo-YAP signaling pathway and contact inhibition of growth. *J. Cell. Sci.* **127,** 709-717.

Guorong Li, Xiaoli Du, William C. Vass, Alex G. Papageorge, Douglas R. Lowy and Xiaolan Qian. (2011). Full activity of the deleted in liver cancer 1 (DLC1) tumor suppressor depends on an LD-like motif that binds talin and focal adhesion kinase (FAK). *Proceedings of the National Academy of Sciences of the United States of America* **108,** 17129-17134.

Haage, A., Goodwin, K., Whitewood, A., Camp, D., Bogutz, A., Turner, C. T., Granville, D. J., Lefebvre, L., Plotnikov, S., Goult, B. T. et al. (2018). Talin autoinhibition regulates cell-ECM adhesion dynamics and wound healing In Vivo. *Cell Reports* **25,** 2401-2416.e5.

Haining, A. W. M., Rahikainen, R., Cortes, E., Lachowski, D., Rice, A., von Essen, M., Hytonen, V. P. and Del Rio Hernandez, A. (2018). Mechanotransduction in talin through the interaction of the R8 domain with DLC1. *PLoS Biol.* **16,** e2005599.

Han, S. J., Dean, K. M., Whitewood, A. J., Bachir, A., Guttierrez, E., Groisman, A., Horwitz, A. R., Goult, B. T. and Danuser, G. (2019). Formation of talin-vinculin pre-complexes dictates maturation of nascent adhesions by accelerated force transmission and vinculin recruitment. *bioRxiv*.

Hemmings, L., Rees, D. J., Ohanian, V., Bolton, S. J., Gilmore, A. P., Patel, B., Priddle, H., Trevithick, J. E., Hynes, R. O. and Critchley, D. R. (1996). Talin contains three actin-binding sites each of which is adjacent to a vinculin-binding site. *J. Cell. Sci.* **109 (Pt 11),** 2715-2726.

Henikoff, S. and Henikoff, J. G. (1992). Amino acid substitution matrices from protein blocks. *Proc. Natl. Acad. Sci. U. S. A.* **89,** 10915-10919.

Huang, H. K., Lin, Y. H., Chang, H. A., Lai, Y. S., Chen, Y. C., Huang, S. C., Chou, C. Y. and Chiu, W. T. (2020). Chemoresistant ovarian cancer enhances its migration abilities by increasing store-operated ca(2+) entry-mediated turnover of focal adhesions. *J. Biomed. Sci.* **27,** 36-5.

Humphrey, W., Dalke, A. and Schulten, K. (1996). VMD: Visual molecular dynamics. *Journal of Molecular Graphics* **14,** 33-38.

Hytonen, V. P. and Vogel, V. (2008). How force might activate talin's vinculin binding sites: SMD reveals a structural mechanism. *PLoS Comput. Biol.* **4,** e24.

Isenberg, G., Doerhoefer, S., Hoekstra, D. and Goldmann, W. H. (2002). Membrane fusion induced by the major lipid-binding domain of the cytoskeletal protein talin. *Biochem. Biophys. Res. Commun.* **295,** 636-643.

Jaalouk, D. E. and Lammerding, J. (2009). Mechanotransduction gone awry. *Nat. Rev. Mol. Cell Biol.* **10,** 63-73.

Jorgensen, W. L. and Madura, J. D. (1983). Quantum and statistical mechanical studies of liquids. 25. solvation and conformation of methanol in water. *Journal of the American Chemical Society* **105,** 1407-1413.

Kim, N. G. and Gumbiner, B. M. (2015). Adhesion to fibronectin regulates hippo signaling via the FAK-src-PI3K pathway. *J. Cell Biol.* **210,** 503-515.

Kopp, P. M., Bate, N., Hansen, T. M., Brindle, N. P., Praekelt, U., Debrand, E., Coleman, S., Mazzeo, D., Goult, B. T., Gingras, A. R. et al. (2010). Studies on the morphology and spreading of human endothelial cells define key inter- and intramolecular interactions for talin1. *Eur. J. Cell Biol.* **89,** 661-673.

Kumar, A., Ouyang, M., Van den Dries, K., McGhee, E. J., Tanaka, K., Anderson, M. D., Groisman, A., Goult, B. T., Anderson, K. I. and Schwartz, M. A. (2016). Talin tension sensor reveals novel features of focal adhesion force transmission and mechanosensitivity. *J. Cell Biol.* **213,** 371-383.

Kumari, R., Kumar, R. and Lynn, A. (2014). g_mmpbsa—A GROMACS tool for high-throughput MM-PBSA calculations. *Journal of chemical information and modeling* **54,** 1951-1962.

Kumper, S., Mardakheh, F. K., McCarthy, A., Yeo, M., Stamp, G. W., Paul, A., Worboys, J., Sadok, A., Jorgensen, C., Guichard, S. et al. (2016). Rho-associated kinase (ROCK) function is essential for cell cycle progression, senescence and tumorigenesis. *Elife* **5,** e12994.

Lai, M. T., Hua, C. H., Tsai, M. H., Wan, L., Lin, Y. J., Chen, C. M., Chiu, I. W., Chan, C., Tsai, F. J. and Jinn-Chyuan Sheu, J. (2011). Talin-1 overexpression defines high risk for aggressive oral squamous cell carcinoma and promotes cancer metastasis. *J. Pathol.* **224,** 367-376.

Lindorff-Larsen, K., Piana, S., Palmo, K., Maragakis, P., Klepeis, J. L., Dror, R. O. and Shaw, D. E. (2010). Improved side-chain torsion potentials for the amber ff99SB protein force field. *Proteins* **78,** 1950-1958.

Liu, X. and Zheng, W. M. (2006). An amino acid substitution matrix for protein conformation identification. *J. Bioinform Comput. Biol.* **4,** 769-782.

Lu, P., Weaver, V. M. and Werb, Z. (2012). The extracellular matrix: A dynamic niche in cancer progression. *The Journal of Experimental Medicine* **209,** i1.

MacKerell, A. D., Bashford, D., Bellott, M., Dunbrack, R. L., Evanseck, J. D., Field, M. J., Fischer, S., Gao, J., Guo, H., Ha, S. et al. (1998). All-atom empirical potential for molecular modeling and dynamics studies of proteins. *The journal of physical chemistry. B* **102,** 3586-3616.

Makoto Nagano, Daisuke Hoshino, Naohiko Koshikawa, Toshifumi Akizawa and Motoharu Seiki. (2012). Turnover of focal adhesions and cancer cell migration. *International journal of cell biology* **2012,** 310616-10.

Malla, R. R. and Vempati, R. K. (2020). Talin: A potential drug target for cancer therapy. *Curr. Drug Metab.*

Meijering, E., Dzyubachyk, O. and Smal, I. (2011). Methods for cell and particle tracking. In *Methods in Enzymology*, pp. 183-200. United States: Elsevier Science & Technology.

Murrell, M., Oakes, P. W., Lenz, M. and Gardel, M. L. (2015). Forcing cells into shape: The mechanics of actomyosin contractility. *Nat. Rev. Mol. Cell Biol.* **16,** 486-498.

Niroula, A., Urolagin, S. and Vihinen, M. (2015). PON-P2: Prediction method for fast and reliable identification of harmful variants. *PloS one* **10,** e0117380.

Rahikainen, R., Ohman, T., Turkki, P., Varjosalo, M. and Hytonen, V. P. (2019). Talin-mediated force transmission and talin rod domain unfolding independently regulate adhesion signaling. *J. Cell. Sci.* **132,** 10.1242/jcs.226514.

Rahikainen, R., von Essen, M., Schaefer, M., Qi, L., Azizi, L., Kelly, C., Ihalainen, T. O., Wehrle-Haller, B., Bastmeyer, M., Huang, C. et al. (2017). Mechanical stability of talin rod controls cell migration and substrate sensing. *Sci. Rep.* **7,** 3571-2.

Sakamoto, S., McCann, R. O., Dhir, R. and Kyprianou, N. (2010). Talin1 promotes tumor invasion and metastasis via focal adhesion signaling and anoikis resistance. *Cancer Res.* **70,** 1885-1895.

Schneider, C. A., Rasband, W. S. and Eliceiri, K. W. (2012). NIH image to ImageJ: 25 years of image analysis. *Nat. Methods* **9,** 671-675.

Sun, Z., Guo, S. S. and Fassler, R. (2016). Integrin-mediated mechanotransduction. *The Journal of Cell Biology* **215,** 445.

Sun, Z., Tseng, H., Tan, S., Senger, F., Kurzawa, L., Dedden, D., Mizuno, N., Wasik, A. A., Thery, M., Dunn, A. R. et al. (2016). Kank2 activates talin, reduces force transduction across integrins and induces central adhesion formation. *Nature cell biology* **18,** 941-953.

Tanentzapf, G. and Brown, N. H. (2006). An interaction between integrin and the talin FERM domain mediates integrin activation but not linkage to the cytoskeleton. *Nat. Cell Biol.* **8,** 601-606.

Tang, Z., Li, C., Kang, B., Gao, G., Li, C. and Zhang, Z. (2017). GEPIA: A web server for cancer and normal gene expression profiling and interactive analyses. *Nucleic Acids Res.* **45,** W98-W102.

Tate, J. G., Bamford, S., Jubb, H. C., Sondka, Z., Beare, D. M., Bindal, N., Boutselakis, H., Cole, C. G., Creatore, C., Dawson, E. et al. (2019). COSMIC: The catalogue of somatic mutations in cancer. *Nucleic Acids Res.* **47,** D941-D947.

Theodosiou, M., Widmaier, M., Bottcher, R. T., Rognoni, E., Veelders, M., Bharadwaj, M., Lambacher, A., Austen, K., Muller, D. J., Zent, R. et al. (2016). Kindlin-2 cooperates with talin to activate integrins and induces cell spreading by directly binding paxillin. *Elife* **5,** e10130.

Wegener, K. L., Partridge, A. W., Han, J., Pickford, A. R., Liddington, R. C., Ginsberg, M. H. and Campbell, I. D. (2007). Structural basis of integrin activation by talin. *Cell* **128,** 171-182.

Yao, M., Goult, B. T., Klapholz, B., Hu, X., Toseland, C. P., Guo, Y., Cong, P., Sheetz, M. P. and Yan, J. (2016). The mechanical response of talin. *Nature communications* **7,** 11966.

Zacharchenko, T., Qian, X., Goult, B. T., Jethwa, D., Almeida, T. B., Ballestrem, C., Critchley, D. R., Lowy, D. R. and Barsukov, I. L. (2016). LD motif recognition by talin: Structure of the talin-DLC1 complex. *Structure* **24,** 1130-1141.

Zhang, X., Jiang, G., Cai, Y., Monkley, S. J., Critchley, D. R. and Sheetz, M. P. (2008). Talin depletion reveals independence of initial cell spreading from integrin activation and traction. *Nat. Cell Biol.* **10,** 1062-1068.

Supplementary Figures

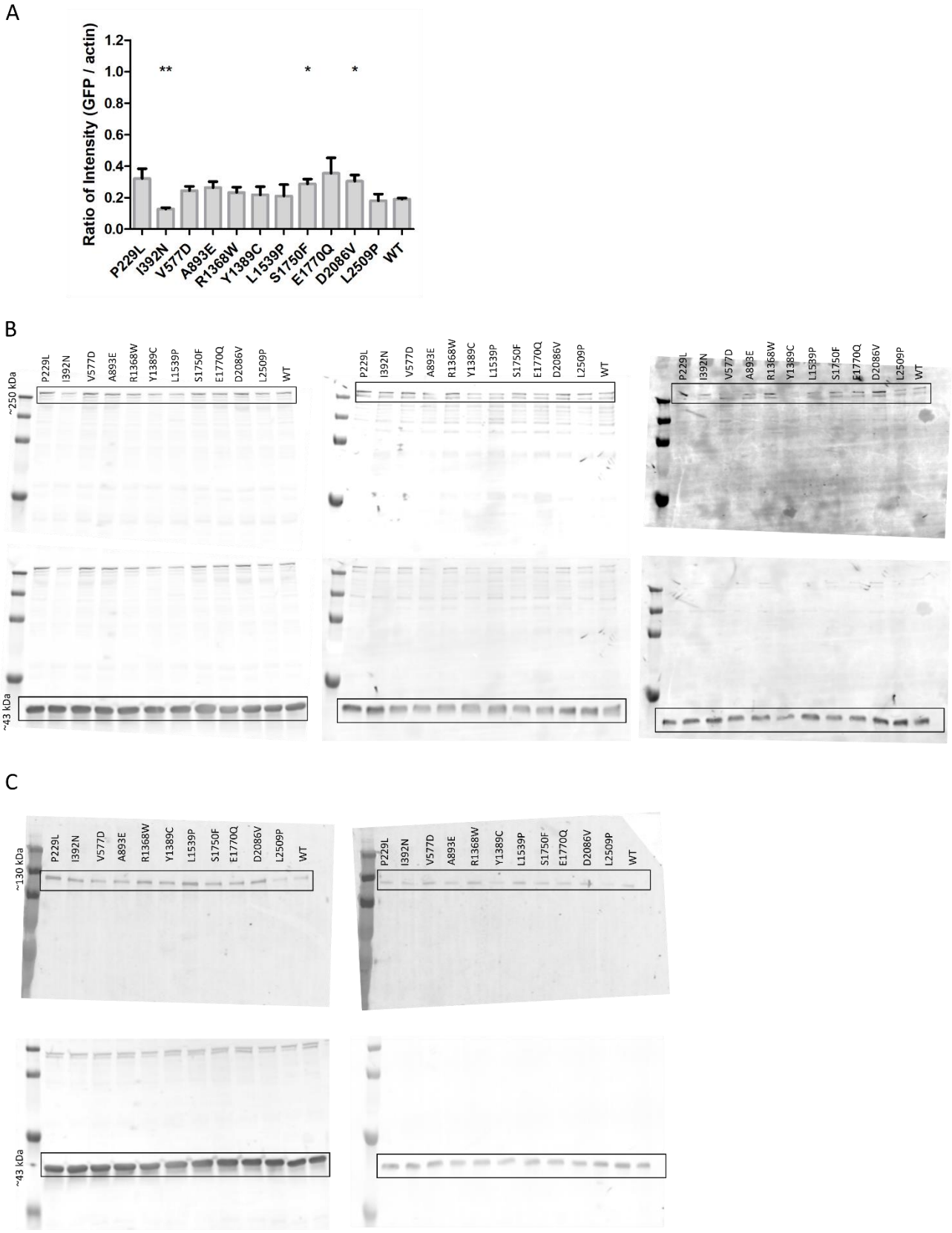

Figure S1: A) Quantification of Western Blots showing talin expression level in the analysed cells (GFP/actin). B) Western Blots used for quantification of talin expression. Blots are immunolabelled against GFP (top) and actin (bottom). C) Western Blots used for quantification of FAKpTyr397. Blots are immunolabelled against FAKpTyr397 (top) and actin (bottom).

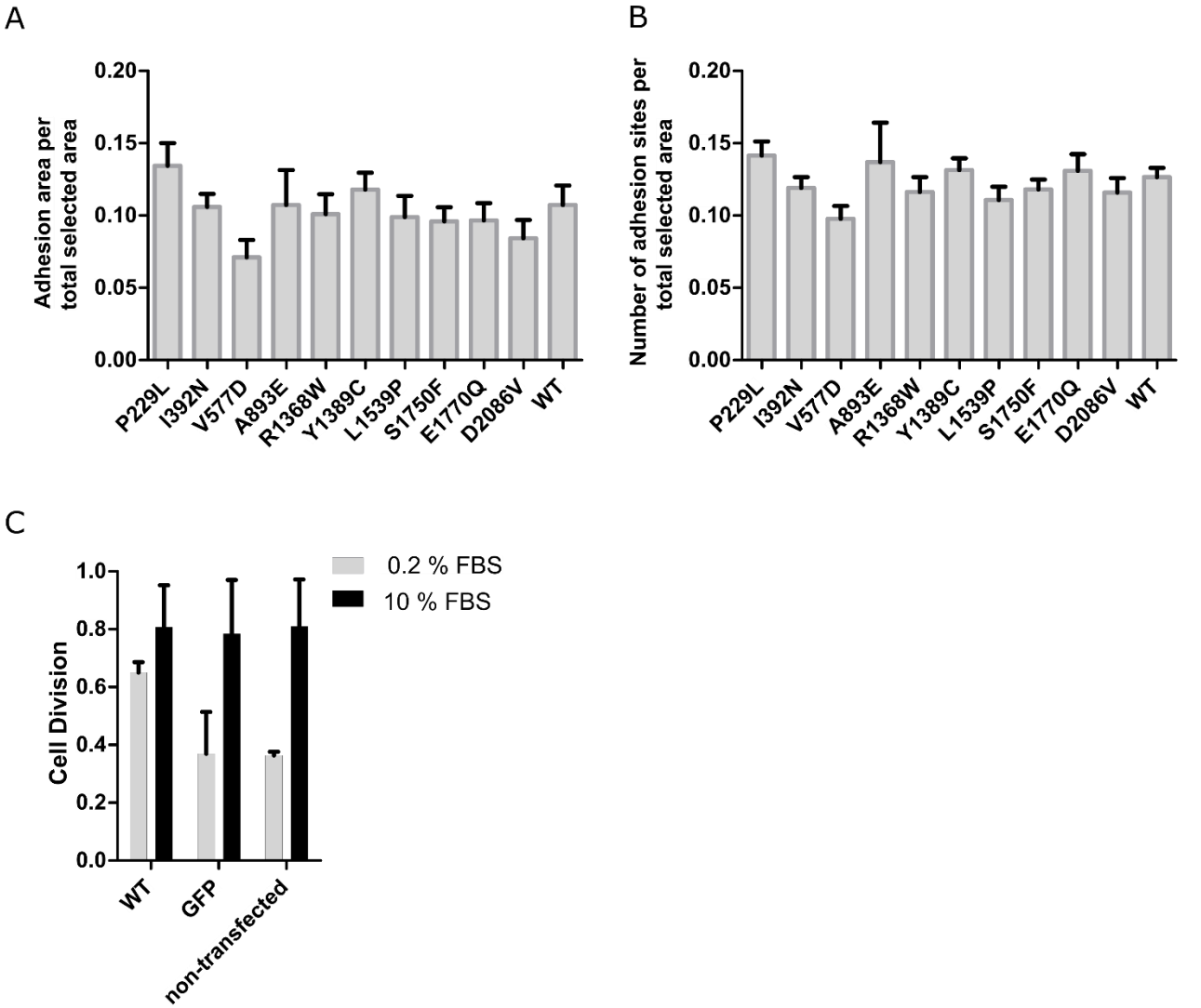

Figure S2: A, B) Graphs showing the results of adhesion site analysis; n~30 cells from two separate experiment. Results are shown as the ratios of adhesion area per total selected area from cell (A) or as number of adhesions per selected area (B). The statistical significance of all results was analysed by one way ANOVA and Bonferroni test: P>0.05, not significant. Due to lack of polarity and seemingly disturbed focal adhesions, L2509P was not included in this analysis (C) Cell division analysis in the presence of 10% FBS and 0.2% FBS defined by the average number of times the cells divide in 12 hours; GFP = transfected mock cells with empty vector; n~ 100 cells from three separate experiment. The statistical analysis was calculated by t-test, non-parametric test of Mann-Whitney: *P<0.05, **P<0.01, ***P<0.001 in comparison to WT for each condition.

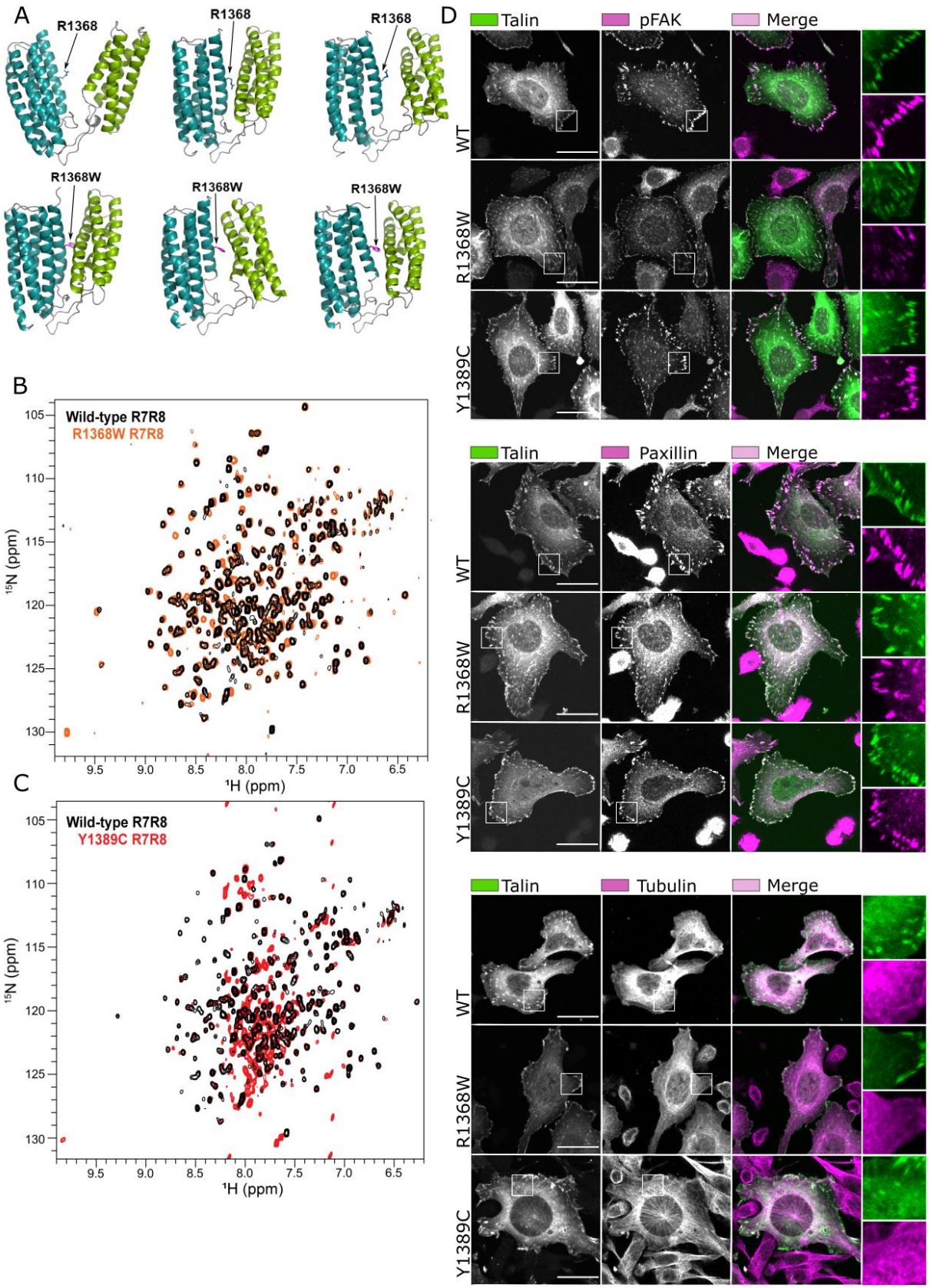

Figure S3: A) Talin rod R7-R8 fragment MD simulations for WT and R1368W. Notice the distance between the domain in the WT and R1368W (B) NMR spectra of R7-R8 WT (black) and R7-R8 R1368W (orange) peaks. (C) NMR spectra of R7-R8 WT (black) and R7-R8 Y1389C (red) peaks. (D) Representative confocal immunofluorescence images of the co-localisation of FA proteins (FAKpTyr397 and paxillin) and tubulin organisation in the cells with talin WT, R1368W and Y1389C. Scale bars are 25 µm, zoom-in square size is 12.5µm x 12.5 µm.

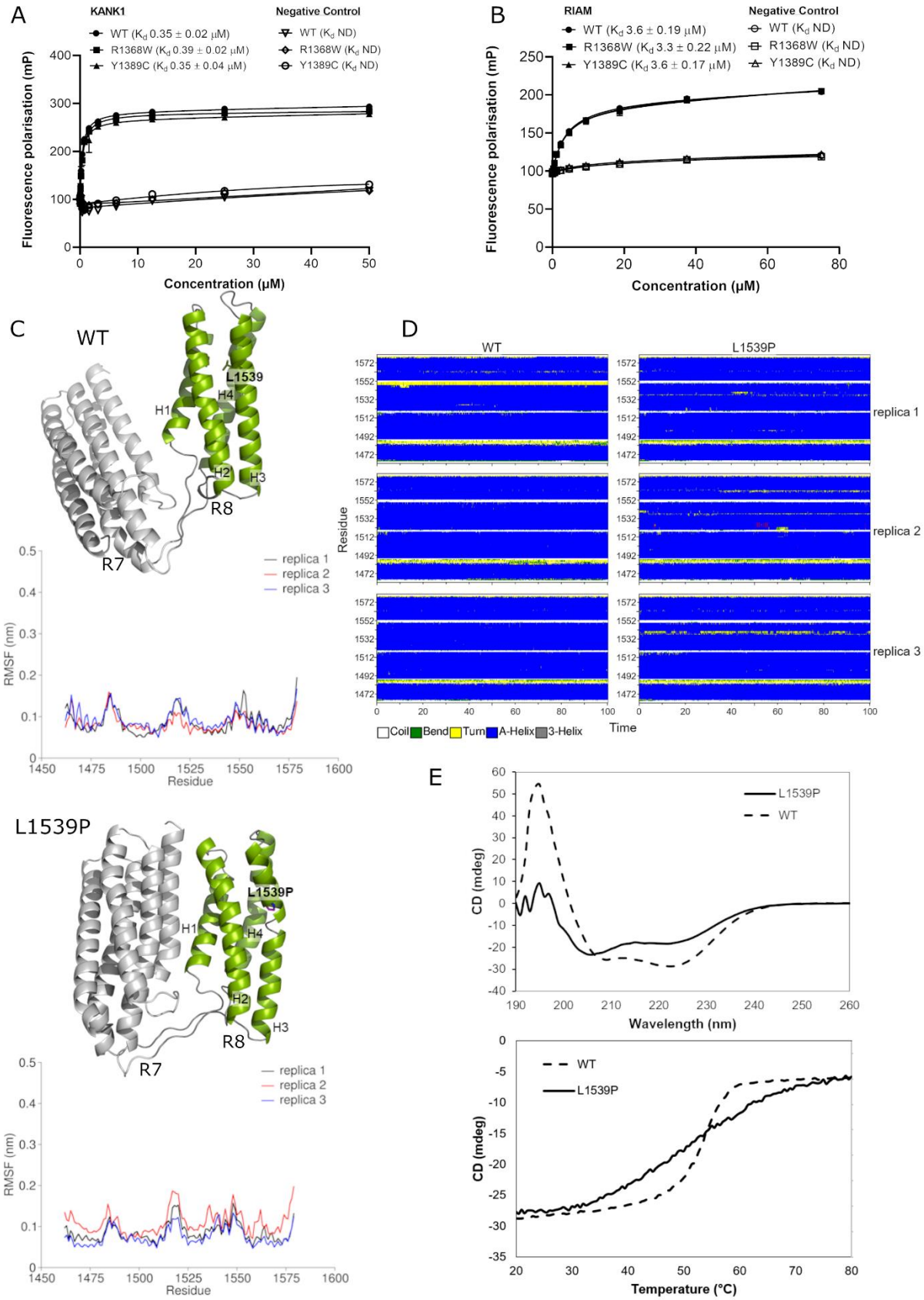

Figure S4: (A, B) Fluorescence Polarisation (FP) for the R7-R8 fragment of WT, R1368W and Y1389C showed no significant changes in the interaction with KANK (A) and RIAM (B). Fluorescence polarisation assays were performed using protein serially diluted from a starting concentration of 75 μM with target RIAM peptide (4-30) concentration at 1 μM, and 60 μM with target KANK1 peptide (30-68) at 1 μM. Measurements were taken using a CLARIOstar plate reader

(BMGLabTech) at 20°C. GraphPad Prism 7 software was used for data analysis with one-site total binding equation used to generate a K_d. (C) MD simulation for L1539P in R8; the R7-R8 was used in the simulations, but the analysis performed on R8. Proline breaks the secondary structure and increase the flexibility of the domain. R7 is shown in grey and R8 in green. (D) Three replicates of the secondary structure analysis (DSSP) run for talin-1 R8 domain in WT and L1539P mutation showing changes in the stability of H3. (E) CD spectra (190-260 nm) and melting temperature analysis (222nm) of R7-R8 WT and L1539P showing a loss of cooperative unfolding for the mutation.

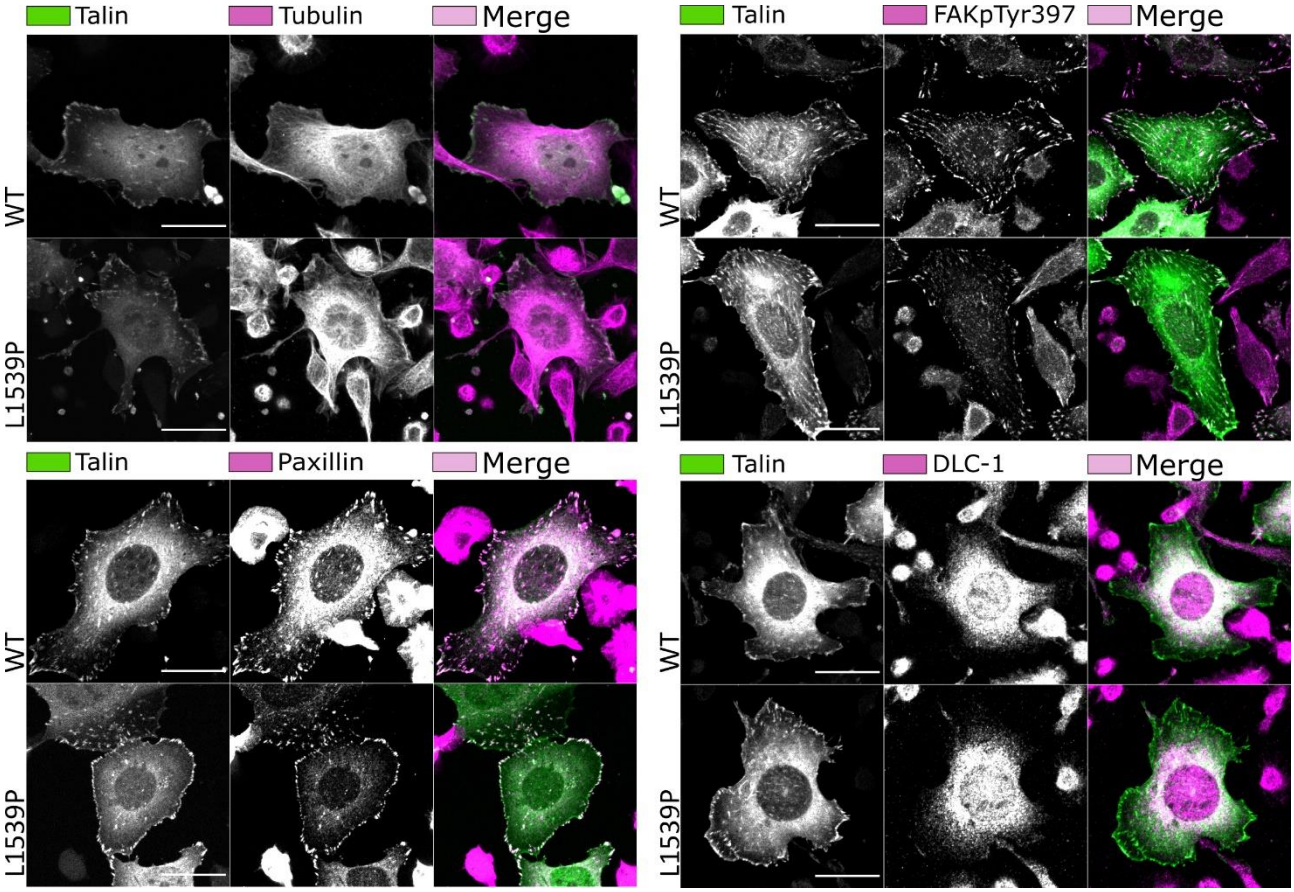

Figure S5: Immunofluorescence analysis for the co-localisation of FA proteins (FAKpTyr397, paxillin), and DLC1 and tubulin in the cells transfected with talin WT and L1539P mutation. Scale bars are 25 µm.

Supplementary Materials and Methods

Screening TLN1 mutations using bioinformatics

In order to classify all mutations into different classes and groups, we used structural information from the protein data bank (PDB): 3IVF (Elliott et al., 2010), 4F7G (Song et al., 2012), 1SJ7 (Papagrigoriou et al., 2004), 2L7A (Goult et al., 2013), 2X0C (Gingras et al., 2010), 2KBB (Goult et al., 2009), 3DYJ (Gingras et al., 2009) and 2QDQ (Gingras et al., 2008). We examined each mutations position on the talin domains and the location on the structure (surface or buried). This was done using an algorithm developed by our group (Nurminen and Hytönen, 2018) and using PyMOL software to visually observe the position of the mutation. The mutations were classified using PON-P2 tool into pathogenic, neutral and unknown to obtain the probability for pathogenicity. PON-P2 is

freely available at http://structure.bmc.lu.se/PON-P2/ (Niroula et al., 2015). The BLOSUM 62 matrix (Henikoff and Henikoff, 1992) was used to evaluate the severity of the mutations. The degree of evolutionary conservation of the amino acid in the talin-1 sequence was investigated using ConSurf (https://consurf.tau.ac.il/ (Ashkenazy et al., 2016)). The amino acid substitution matrices CBSM60 was used to analyse the sequence-structure relationship of the protein (Liu and Zheng, 2006). We also investigated whether the mutation was located in known ligand-binding sites and reported the recurrence and the substitution of the amino acid from hydrophobicity to hydrophilicity and vice versa. The mutations were classified into six group based on their location: surface, buried, on a loop, on a linker but buried, between the helices buried, and on the dimerisation domain. These were given the position code of 0.4, 1, 0.2, 1, 0 and 0.8 respectively. For the change in polarity, we gave a score of one when the amino acid was mutated from hydrophilic residue to hydrophobic residue or from hydrophobic residue to hydrophilic residue. Considering all these variables, we estimated the scoring coefficient according to the importance feature of each factor using formula $n_1X1+n_2X2+\ldots+n_nXn$ (n is the scoring coefficient and X is the variable). We tried multiple scoring factor combinations to obtain mutations appearing most frequently with a high score. Finally, we generated a table from which we selected ten mutants predicted to represent the most drastic mutations based on "total score". The scoring coefficient to calculate the "total score" of one iteration in Table 1 is as follows: 2*(location within the subdomain code) + 0*(ligand binding code) + 4*(ConSurf code) + 0*(BLOSUM 62) + 2*(PON-P2) 1* (CBSM60) + 0.05*(polarity change from hydrophilic to hydrophobic) + 0.4*(polarity change from hydrophobic to hydrophilic). Altogether, nine iterations were done.

Prediction of the deleterious effect of mutation

We normalised the score for each investigated amino-acid substitution between zero and one, with one being the most deleterious. Considering all these factors, we calculated a final score using equation $n_1X1+n_2X2+\ldots+n_nXn$ by giving different indexes (scoring coefficient, n) a range of zero to five, where a higher value indicated a greater effect of the variant. Using the variables (X), "location within the subdomain", "ligand binding", "ConSurf", "BLOSUM62", "PON-P2", "CBSM60" and "polarity change" we tested different relative weightings (for example 2, 0, 4, 0, 2, 1, 0.05, 0.4) and ran nine iterations. Each time, we pooled the top 10 mutations which had the highest score. Based on these criteria, 78 mutants received a score above five, and 10 mutations with the highest scores (>7) likely to be detrimental were taken forward for further analysis.

Antibodies

Table S1: Antibodies used in this study. Antibodies were diluted in 1.5% BSA, 0.1% Triton-X /PBS buffer. Appropriate secondary antibodies from LI-CORE and a LI-CORE imaging system was used.

Antibody	**Manufacturer**	**Method**	**Dilution used**
anti-vinculin	Merck, clone hVIN, V9131, RRID:AB_477629	Immunostaining/ Western blot	1:100 / 1:1000
anti-FAK-pY397	Abcam, ab81298 [EP2160Y], RRID:AB_1640500	Immunostaining/ Western blot	1:100 / 1:1000
anti-paxillin	BD Biosciences, 349/Paxillin, 610051, RRID:AB_397463	Immunostaining/ Western blot	1:100 / 1:1000
GFP antibody	Sicgen AB0020-200	Western blot	1:1000
Actin	Millipore, MAB 1501R, RRID: AB_2223041	Western blot	1:2000
Alexa Fluor 568 phalloidin	Life Technologies	Immunostaining	1:40
Alexa Fluor 568 goat anti-rabbit IgG	Life Technologies A11011	Immunostaining	1:200
Alexa Fluor 568 goat anti-mouse IgG	Molecular probes, A11004	Immunostaining	1:200

Image analyses

Protein expression level and co-localisation quantification from confocal images. For the quantification of expression level of proteins, the total intensity signal was determined from transfected cells. For the co-localisation quantification of protein intensity, 10-15 adhesion sites per cell were selected based on the EGFP-talin channel using circular selection (0.7 µm) of ImageJ and selection was copied to the red fluorescence channel. Background was assessed from the EGFP channel using circular selections (2.2 µm) from areas devoid of EGFP signal and these areas were again copied to the red fluorescence channel. Protein expression and co-localisation was measured using ImageJ.

Analyses of adhesion size and number. To determine the adhesion size and number in transfected cells, we conducted particle analysis using ImageJ particle analyser. First, the threshold range was set to clear out the background noise. Then we selected areas from cell boundaries (roughly one third of the cell membrane) and analysed the adhesions sites based on the signal from the EGFP channel. Cut-off sizes of < 0.1 and > 20 μm^2 were used in the analyses. Results are shown as ratio of adhesion area and as the number of individual adhesions sites per total selected area per.

Supplementary References

Ashkenazy, H., Abadi, S., Martz, E., Chay, O., Mayrose, I., Pupko, T. and Ben-Tal, N. (2016). ConSurf 2016: An improved methodology to estimate and visualize evolutionary conservation in macromolecules. *Nucleic Acids Res.* **44,** 344.

Elliott, P. R., Goult, B. T., Kopp, P. M., Bate, N., Grossmann, J. G., Roberts, G. C., Critchley, D. R. and Barsukov, I. L. (2010). The structure of the talin head reveals a novel extended conformation of the FERM domain. *Structure* **18,** 1289-1299.

Gingras, A. R., Bate, N., Goult, B. T., Hazelwood, L., Canestrelli, I., Grossmann, J. G., Liu, H., Putz, N. S., Roberts, G. C., Volkmann, N. et al. (2008). The structure of the C-terminal actin-binding domain of talin. *EMBO J.* **27,** 458-469.

Gingras, A. R., Bate, N., Goult, B. T., Patel, B., Kopp, P. M., Emsley, J., Barsukov, I. L., Roberts, G. C. and Critchley, D. R. (2010). Central region of talin has a unique fold that binds vinculin and actin. *J. Biol. Chem.* **285,** 29577-29587.

Gingras, A. R., Ziegler, W. H., Bobkov, A. A., Joyce, M. G., Fasci, D., Himmel, M., Rothemund, S., Ritter, A., Grossmann, J. G., Patel, B. et al. (2009). Structural determinants of integrin binding to the talin rod. *J. Biol. Chem.* **284,** 8866-8876.

Goult, B. T., Bate, N., Anthis, N. J., Wegener, K. L., Gingras, A. R., Patel, B., Barsukov, I. L., Campbell, I. D., Roberts, G. C. and Critchley, D. R. (2009). The structure of an interdomain complex that regulates talin activity. *J. Biol. Chem.* **284,** 15097-15106.

Goult, B. T., Zacharchenko, T., Bate, N., Tsang, R., Hey, F., Gingras, A. R., Elliott, P. R., Roberts, G. C., Ballestrem, C., Critchley, D. R. et al. (2013). RIAM and vinculin binding to talin are mutually exclusive and regulate adhesion assembly and turnover. *J. Biol. Chem.* **288,** 8238-8249.

Henikoff, S. and Henikoff, J. G. (1992). Amino acid substitution matrices from protein blocks. *Proc. Natl. Acad. Sci. U. S. A.* **89,** 10915-10919.

Liu, X. and Zheng, W. M. (2006). An amino acid substitution matrix for protein conformation identification. *J. Bioinform Comput. Biol.* **4,** 769-782.

Niroula, A., Urolagin, S. and Vihinen, M. (2015). PON-P2: Prediction method for fast and reliable identification of harmful variants. *PloS one* **10,** e0117380.

Nurminen, A. and Hytönen, V. P. (2018). StructureMapper: A high-throughput algorithm for analyzing protein sequence locations in structural data. *Bioinformatics* **34,** 2302-2304.

Papagrigoriou, E., Gingras, A. R., Barsukov, I. L., Bate, N., Fillingham, I. J., Patel, B., Frank, R., Ziegler, W. H., Roberts, G. C., Critchley, D. R. et al. (2004). Activation of a vinculin-binding site in the talin rod involves rearrangement of a five-helix bundle. *EMBO J.* **23,** 2942-2951.

Song, X., Yang, J., Hirbawi, J., Ye, S., Perera, H. D., Goksoy, E., Dwivedi, P., Plow, E. F., Zhang, R. and Qin, J. (2012). A novel membrane-dependent on/off switch mechanism of talin FERM domain at sites of cell adhesion. *Cell Res.* **22,** 1533-1545.